Nonlinear feedback control of bimodality in the wake of a three-dimensional bluff body

D. Ahmed* and A. S. Morgans†
Department of Mechanical Engineering, Imperial College London, London SW7 2AZ, United Kingdom

(Received 9 March 2022; accepted 14 July 2022; published 22 August 2022)

The turbulent wake behind a square-back Ahmed body in close proximity to the ground exhibits bimodal switching. This manifests as the center of the wake switching between one of two asymmetric positions, either horizontally or vertically. Switches occur over random timescales, with the wake recovering symmetry in the long time average. The present work employs wall-resolved large eddy simulations to investigate feedback control for suppressing horizontal (lateral) wake bimodality of a square-back Ahmed body at Reynolds number, $\mathrm{Re}_H \sim 3.3 \times 10^4$ based on the body height. Base-mounted pressure sensors are used to estimate the position of the wake as an input signal for the controller, while actuation targets the near-wake region via synthetic jets emanating from a gap around the perimeter of the Ahmed body base. A nonlinear feedback controller based on a Langevin model of the wake dynamics is synthesized. This successfully suppresses the wake lateral bimodal switching. However, this switching is replaced by a time-periodic streamwise motion of the large coherent structure occupying the near-wake region, leading to amplification of the higher frequency dynamical wake modes. The action of feedback control also leads to base pressure recovery and a reduction in pressure drag. Upon varying the controller parameters, a trade-off between the degree of bimodality suppression and drag reduction is observed. A maximum drag reduction of 7.4% is achieved for a semisymmetrized wake, with a fully symmetrized wake achieving 2.5% reduction. Bimodality suppression is proposed to have an indirect link to drag reduction through the effect of the wake state on the separated free shear layers and the upstream boundary layers.

DOI: 10.1103/PhysRevFluids.7.084401

I. INTRODUCTION

The relevance of bluff bodies to the transportation industry drives the need for bluff body aerodynamic drag reduction. Ground vehicles such as lorries, buses, and light-duty vehicles are classified as bluff bodies. Sudin *et al.* [1] indicated that the aerodynamic drag consumes 50% of the total fuel burnt by a passenger car at typical highway speeds, compared to 65% for trucks, as reported by Seifert *et al.* [2]. The drag force exerted on a solid body moving in a fluid stream is classified into pressure drag and friction drag [3]. The former is related to the pressure difference between the frontal and rear sections of the body in the streamwise direction, while the latter is associated with the friction between the surfaces of the solid body and the moving fluid, i.e., the development of boundary layers. For bluff bodies, pressure drag (also known as form drag) dominates, constituting approximately 80% of the total drag in case of flow past an Ahmed body [4].

*d.ahmed18@imperial.ac.uk
†a.morgans@imperial.ac.uk

The pressure drag of a bluff body largely arises due to the pressure deficit on the rear part of the body caused by large-scale flow separation. It depends on the location of flow separation as well as the dynamics and topology of the wake flow downstream of the body. For three-dimensional (3D) bluff bodies whose flow separation position is fixed, including axisymmetric [5,6] and rectilinear [4,7,8] bluff bodies, some key common dynamical features can be identified. These include the development of boundary layers along the body surfaces, which separate at the rear edges of the body, creating free shear layers which bound the recirculation region in the near wake. The recirculation region extends from the rear part of the body up to the so-called free stagnation point. The shear layers experience Kelvin-Helmholtz instability, thus amplifying disturbances in the wake downstream of the body. The interaction between each parallel pair of separated shear layers leads to coherent vortex shedding in the wake [9]. The whole recirculation region also exhibits a pumping motion in the streamwise direction, which is associated with oscillations of the free stagnation point in the wake [7]. Instabilities related to symmetry breaking are also observed in the wake of 3D bluff bodies, which will be discussed in further detail.

The present study considers a 3D blunt bluff body in the form of the square-back Ahmed body, representing a simplified road vehicle geometry. The time-averaged wake topology and characteristic frequencies of the square-back Ahmed body were the focus of early studies by Ahmed *et al.* [4] and Mason and Beebe [10] and are now well established. A further unsteady wake behavior has recently been identified [11,12], known as bimodality or bistability. It manifests as random switching of the wake between off-centered (asymmetric) preferred positions. While the time-averaged turbulent wake exhibits symmetry, instantaneously the wake exhibits a random switching between two asymmetric states, with the timescales between switching events being relatively long. Similar wake symmetry-breaking behavior has been observed in the wakes of other bluff bodies. The laminar flow past a sphere at sufficiently high Reynolds number exhibits axisymmetry breaking in the wake, which increases the drag, the degree of increase increasing with Reynolds number [13]. The laminar wakes of blunt-based axisymmetric bodies similarly transition from axisymmetry to a planar symmetry as Reynolds number increases past a critical value. For turbulent wake conditions, this rotational symmetry breaking is preserved, with a random dynamical behavior in the azimuthal position of the symmetry plane [5]—this is known as multimodality or multistability. A similar behavior is observed in the turbulent wake of the sphere [6]. Compared to axisymmetric bodies, the symmetry of the base surface of the square-back Ahmed body, permits only two azimuthal positions of the wake, promoting bimodality instead of multimodality.

The wake of a square-back Ahmed body evolves according to a similar symmetry pattern to that for axisymmetric bodies. In the laminar flow regime, reflectional symmetry breaking (RSB), first occurs when the Reynolds number exceeds a critical value. This value has been experimentally found to be 365 (based on body height) for the square-back Ahmed body with a ground proximity of 60% of the body height [12]. The steady symmetric state of the wake transitions to steady asymmetric after a short unsteadiness period. The wake maintains this asymmetric state at higher Re numbers in the laminar flow regime. As Reynolds number increases, an unsteady bifurcation emerges, causing periodic vortex shedding in the wake. The same laminar flow sequence of RSB was captured numerically by Evstafyeva *et al.* [14]. In the turbulent regime, the RSB static modes arising from the laminar flow bifurcations have been shown to persist. However, turbulent perturbations now cause the wake to switch randomly between off-centered preferred positions [15]. The wake resides at one stable asymmetric position until it is sufficiently perturbed to be able to switch to the other reflected position. This behavior is found to be Re-independent in the turbulent flow regime up to a value of at least Re of 3×10^6, matching the scale of real road vehicles in driving conditions [16]. The associated topology shift is the skewness of the near-wake toroidal vortex towards and away from the base surface [11,17,18]. The instantaneous asymmetric position of the wake is correlated with the proximity of one of the sides of the toroidal-vortex structure to the base.

Bimodality or random RSB in the wake has been the subject of several recent experimental studies [11,12,16,19–23]. It is a unidirectional behavior that occurs in either the horizontal (side-to-side) or vertical (top-to-bottom) direction, depending on the aspect ratio of the body base, the ground

proximity and the yaw angle. Grandemange *et al.* [16] mapped the direction of the bimodality, for a 0° yaw angle, as a function of the base aspect ratio and the ground clearance. Three regimes were identified, depending on the ground clearance normalized by the body width, C^*. For low ground clearances, $C^* < 0.05$, horizontal switching occurs for $0.3 < H/W < 0.65$, where H and W are the base height and width, respectively. For slighter larger ground clearances, $0.05 < C^* < 0.09$, wake switching is inhibited, as a result of the detachment of the under-body flow. For $C^* > 0.09$, bimodal switching occurs in the direction of the longest edge. Plumejeau *et al.* [23] recently investigated the effect of the under-body flow on the interactions of the wake dynamics, noting that the transition of the wake to bimodal was accompanied by a change in the frequency of the vortex shedding mode. Barros *et al.* [24] investigated the sensitivity of the wake dynamics to disturbances induced in the under-body flow, introducing a coupling based on Langevin dynamics between the vertical wake asymmetry and the horizontal bimodality.

In terms of numerical investigations, Rao *et al.* [25] captured the asymmetry of the turbulent wake past the Ahmed body, using the unsteady partially averaged Navier-Stokes (PANS) simulations. Eddy-resolving techniques employing large eddy simulations (LES) and detached eddy simulations (DES) captured the spatial symmetry breaking of the wake but not the switching [26–29]. Dalla Longa *et al.* [18] was the first numerical study which captured the bimodal switching behavior of the wake behind 3D blunt bluff bodies: a square-back Ahmed body and a lorry model. The study employed wall-resolved LES to simulate the flow. It suggested that wake switching events are associated with a stochastic shedding of a hair pin vortex in the near-wake region. The LES study by Hesse and Morgans [30] further suggested that the upstream separation bubble just aft of the body nose is generates disturbances linked to the wake switching. The direct numerical simulation (DNS) results by Podvin *et al.* [31] captured the deviation of the wake and indicated the same dynamics shown in the LES results except bimodality.

Wake bimodality has been found to have implications for drag. The experimental study by Grandemange *et al.* [11] found that wake bimodality contributes up to 9% to pressure drag and creates unfavorable side forces and moments that affect the stability of the body. Haffner *et al.* [22] showed that the averaged base pressure coefficient reduced by 9% during the switching events of the wake compared to the asymmetric wake. The wake is instantaneously symmetric during these switching events, indicating that wake resymmetrization has a favorable effect on the base pressure and consequently the pressure drag. The sensitivity of the friction drag to bimodality suppression has not as yet been investigated, to the best of the authors' knowledge, with most previous studies presuming that the wake state affects the drag via base pressure recovery.

The effect of wake resymmetrization on drag has been exploited in passive and active flow control studies. In terms of passive control, Evrard *et al.* [32] used a base cavity to suppress wake bimodal switching, achieving a 9% drag reduction, while Grandemange *et al.* [33] positioned a vertical cylinder in the center of the recirculation region, preserving wake symmetry and reducing drag by 5%. Active flow control studies which target wake symmetrization have so far achieved much smaller drag reductions than the above passive control approaches. This may be due to the restriction of forcing with body-mounted actuators, as Grandemange *et al.* [33] suggested that the most receptive region for actuating the wake is the center of the recirculation region. The experimental study by Brackston *et al.* [21] used linear feedback control to resymmetrize a turbulent wake, reducing the drag by around 2%. An opposition control strategy was experimentally applied by Li *et al.* [34] to symmetrize the wake; feedback control based on harmonic forcing successfully symmetrized the wake but promoted lateral vortex shedding, limiting the drag reduction to be only slight. Schmidt *et al.* [35] showed that active control could suppress both bimodality and higher frequency dynamics, but the bubble pumping mode persisted. In most cases, the use of linear feedback control to suppress bimodality was found to significantly augment wake fluctuations around the center, as compared to the original fluctuations around the uncontrolled asymmetric position. Additionally, forcing the flow in the near-wake region enhances turbulent activity in the free shear layers, promoting high-frequency dynamics in the wake and also inhibiting drag reduction.

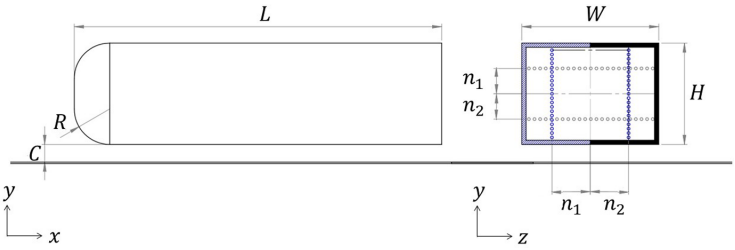

FIG. 1. Ahmed body scaled by one fourth, with height $H = 72$ mm. The circles on the base show the sensor positions used to calculate the vertical (gray) and horizontal (blue) pressure gradients. Actuation is via synthetic jets placed around the base perimeter with a thickness of $0.04H$; actuation is antisymmetric in z as shown by the blue dashed and the black solid areas.

In this paper, we investigate the potential of a nonlinear single-output (SISO) feedback control approach for suppressing the side-to-side wake bimodal switching. To the best of the authors' knowledge, this is the first attempt at applying a nonlinear control approach to the 3D wake of a square-back Ahmed body. High-fidelity, wall-resolved LES are used to simulate the dynamics of the turbulent wake, to implement the nonlinear feedback control and to investigate the effect of the controller on the wake bimodality, the wake dynamics more generally, and the drag. The feedback control setup employs base pressure sensing and synthetic jet actuation through a small gap around the perimeter of the base. The controller is based upon a reduced order model employing the Langevin equation, adapted for a rectilinear geometry. This model, developed by Rigas *et al.* [15] for an axisymmetric body and adapted for rectilinear bodies by Brackston *et al.* [21], accurately captures the evolution of wake reflectional symmetry breaking and random bimodal switching. The paper discusses the simulation setup in Sec. II and the wake dynamics of the unforced case in Sec. III. Section IV provides the details of the model for wake bimodality. The design methodology of the nonlinear feedback controller is provided in Sec. V. The effect of the feedback control on the bimodality, drag, and wake dynamics is presented in Sec. VI. A sensitivity study of the controller nonlinearity on bimodality suppression and the flow properties is further investigated in Sec. VII. Finally, a comparison of the flow field between the unforced and the controlled cases is preformed using modal reduction (proper orthogonal decomposition) and is shown in Sec. VIII.

II. SIMULATION SETUP

Wall-resolved LES is used to simulate the turbulent wake downstream of a square-back Ahmed body and as a test bed for the nonlinear feedback control approach. The dimensions of the square-back Ahmed body are similar to those used by Ahmed *et al.* [4], scaled by one quarter, as shown in Fig. 1. The aspect ratio of the body cross section is $W/H = 1.35$, where W and H are the body width and height, respectively. The length of the body is $L^* = L/H = 3.63$. The clearance between the bottom surface of the body and the ground is $C^* = C/H = 0.174$. The frontal part is rounded with a radius of $R^* = R/H = 0.35$. The Reynolds number based on the body height is $\mathrm{Re}_H = 3.3 \times 10^4$. The solution domain is $(L_{\mathrm{inlet}}, L_x, L_y, L_z) = (2L, 8L, 2L, 2L)$, where $L_{\mathrm{inlet}}, L_x, L_y$, and L_z are the domain length upstream of the body, total domain length in the streamwise direction, transverse domain length, and domain length in the spanwise direction, respectively, as shown in Fig. 2. The blockage factor, defined as the ratio of the Ahmed body cross section to the domain cross section, is 2.5%, small enough to neglect confinement effects. The size of the domain has been chosen according to ERCOFTAC recommendations [36,37].

The inflow used is a steady uniform velocity profile corresponding to the value of Re_H. A no-slip boundary condition is used on the ground and the body surfaces, with a free-slip condition set on the domain sides. A convective outlet condition is set on the domain outlet to avoid backflow. The OpenFOAM CFD toolbox (version 6.0 [38]), employing a finite volume formulation, was used

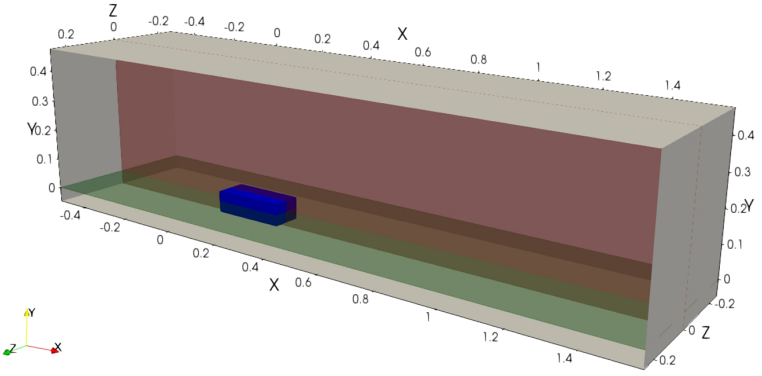

FIG. 2. Solution domain with a vertical body-centered plane (red) and horizontal body-centered plane (green). Point (0,0,0) is located on the base center.

for the simulations. The governing incompressible Navier-Stokes equations are solved using the PIMPLE algorithm, which is a hybrid algorithm of the Pressure Implicit with Splitting of Operators (PISO) and Semi-Implicit Method for Pressure-Linked Equations (SIMPLE) algorithms. The LES employs the Wall-Adapting Local Eddy-viscosity (WALE) model to account for turbulence at subgrid scales [39]. Second-order spatial and temporal discretization schemes were employed.

Unstructured hexahedral cells were used employing the trimmer cells model in StarCCM+ software. This creates hexahedral cells in the solution domain, trimming the mesh core at the boundaries to form polyhedral cells. The prism layers model was used near the solid surfaces to create orthogonal cells, resolving the near-wall flow, as indicated in Figs. 3 and 4. Three different computational grids of 9,11, and 15 million cells were considered. The refinement criteria were based on minimizing the cell sizes in the prism layers, the refined region around the body, and the far-field region. The mesh near the wall, in the prism layers, is refined to fully resolve the boundary layer for each of the three computational grids, maximizing the surface region over which $\overline{y^+} \leqslant 1$, as shown in Fig. 5 for the case of 11×10^6 cells. The normalized near-wall grid sizes in the streamwise and spanwise directions are $\overline{x^+} \leqslant 39$ and $\overline{z^+} \leqslant 40$, respectively, following the mesh requirement for LES [40]. A growth rate of 1.1 is used between the different mesh zones, as shown in Figs. 3 and 4, to minimize the computational cost [30].

For each of the three computational grids, the values of the body drag coefficient, $\overline{C_D}$, the average base pressure, $\overline{C_{\mathrm{PBase}}}$, and the normalized length of the recirculation region, $\frac{\overline{L_R}}{H}$, were calculated and compared to the experiments of Grandemange *et al.* [16], conducted at $\mathrm{Re}_H \sim 3.3 \times 10^4$, and

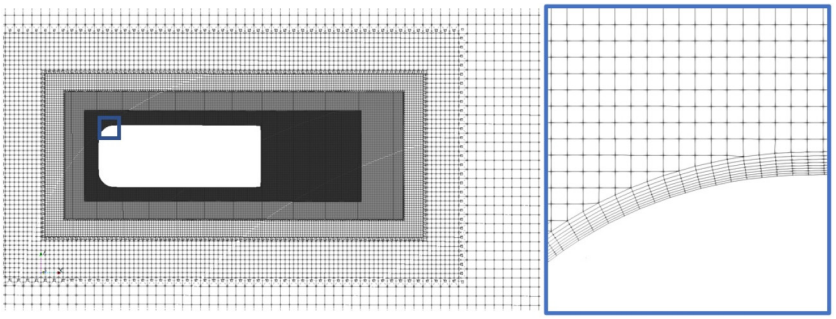

FIG. 3. Mesh details on the vertical plane (xy). The zoomed view (in the blue box) shows the prism layers on the body surface.

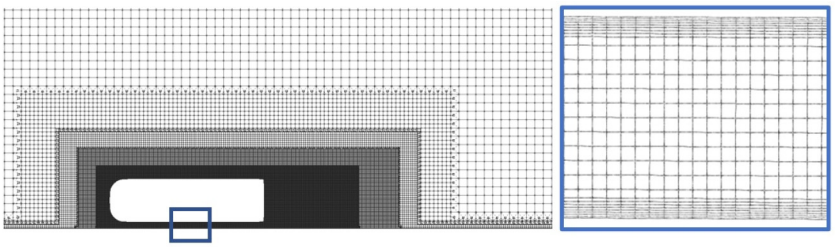

FIG. 4. Mesh details on the horizontal plane (xz). The zoomed view (in the blue box) shows the prism layers used to resolve the boundary layers on both the body and the ground surfaces.

the numerical study of Hesse and Morgans [30]. The maximum deviation from the experimental values for the length of the recirculation region and the average base pressure were about 2% and 15%, respectively. For the latter, it is noted that the deviation from the experimental results of Fan *et al.* [41] is just 4%, suggesting that experimental values for the base pressure span a range. All three values are comparable to the simulation results of Hesse and Morgans [30]. Based on these comparisons and the values of y^+_{max} shown in Table I, the midsize computational grid with 11 million cells is selected for the simulations. The value of $y^+_{\mathrm{Max}} \leqslant 1$, confirming that the near wall regions are fully resolved. We further note that the average cell size in the wake region resolves the Taylor microscale, which represents the minimum turbulent length scale to be resolved by the LES [42].

Having validated the LES approach for accurately simulating the wake flow, we now describe the adaptations to the simulations needed in order to implement feedback control. The feedback control setup employs base pressure sensing and synthetic jet actuation through a small gap around the perimeter of the base, as shown in Fig. 1. For the actuation, a time-dependent boundary condition is needed (only) at the location of the actuator slots. The actuation signal, given by the controller output value, must be calculated at each time step in response to the time-varying input sensor signal from the pressure probes. This is implemented using the SWAK4FOAM (SWiss Army Knife for OpenFOAM) library [43]. SWAK4FOAM is a plug-in C++ library, which allows the use of a user-defined time-varying equation to prescribe the values at the boundary, instead of the default constant value in OpenFOAM.

The drag and pressure coefficients used in analyzing the data in the following sections are calculated as shown in Eqs. (1) and (2), respectively. $D(t)$, ρ and U_∞ represent the drag force, air density and free stream velocity respectively. $P(x, y, z, t)$ represents the pressure at a position (x, y, z) in space at an instant t and P_∞ is the free stream pressure. The spatial gradient of the pressure coefficient in direction n is calculated as shown in Eq. (3), where n represents a cross-flow direction (y, z). n_1 and n_2 are the distances between the base pressure probes (either side of the base

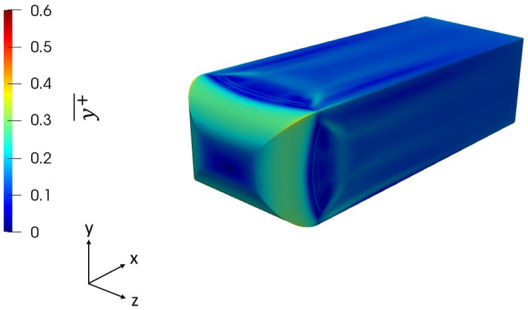

FIG. 5. $\overline{y^+}$ distribution on the Ahmed body.

TABLE I. Mesh independence study, based on the time-averaged drag ($\overline{C_D}$), time-averaged base pressure ($\overline{C_{\mathrm{Pbase}}}$), time-averaged recirculation length ($\overline{L_R}$), and time-averaged and maximum y^+.

Mesh size ($\times 10^6$ cells)	$\overline{C_D}$	$\overline{C_{\mathrm{PBase}}}$	$\frac{\overline{L_R}}{H}$	$\overline{y^+}$	y^+_{Max}
15	0.362	−0.22	1.43	0.10	0.6
11	0.360	−0.22	1.42	0.58	1.0
9	0.352	−0.20	1.45	0.95	3.0
Exp. [16]	–	−0.19	1.41	–	–
Sim. [30]	0.364	−0.20	1.42	–	<1

center line) and the center of the base in the direction n, M is the number of the probes, and N is the total length of the base in the same direction, as shown in Fig. 1:

$$C_D(t) = \frac{D(t)}{\frac{1}{2}HW\rho{U_\infty}^2}, \tag{1}$$

$$C_P(x, y, z, t) = \frac{P(x, y, z, t) - P_\infty}{\frac{1}{2}\rho{U_\infty}^2}, \tag{2}$$

$$\frac{dC_P(t)}{dn} = \frac{\sum_M C_P(n_1, t) - \sum_M C_P(n_2, t)}{\frac{M(n_1+n_2)}{N}}. \tag{3}$$

The momentum coefficient C_μ is defined as the ratio of momentum imposed through the actuators to the free stream momentum and is given by Eq. (4). Equation (5) is used to calculate the actuation power $Pw_{\mathrm{actuation}}$, where $\overline{U_{\mathrm{jet}}}$ and η_{actuator} represent the time-averaged jet velocity and the efficiency of the actuator, respectively. The total power saved due to drag reduction, Pw_{saved}, is calculated as shown in Eq. (6), where ΔF_{drag} is the change in the drag force:

$$C_\mu(t) = \frac{A_{\mathrm{actuator}}\overline{U^2_{\mathrm{jet}}}}{A_{\mathrm{base}}U^2_\infty}, \quad A_{\mathrm{actuator}} = W_{\mathrm{actuator}}\,H, \quad A_{\mathrm{base}} = W\,H, \tag{4}$$

$$Pw_{\mathrm{actuation}} = \frac{A_{\mathrm{actuator}}}{\eta_{\mathrm{actuator}}}\frac{\rho\overline{U^3_{\mathrm{jet}}}}{2}, \tag{5}$$

$$Pw_{\mathrm{saved}} = \Delta F_{\mathrm{drag}}U_\infty. \tag{6}$$

III. UNFORCED FLOW

The spatial gradients of the pressure coefficient on the base of the Ahmed body are used to characterize wake bimodality. Figure 6 depicts the instantaneous gradient of the pressure coefficient in the horizontal (spanwise) and vertical (transverse) directions, denoted as $\partial C_p/\partial z$ and $\partial C_p/\partial y$, respectively, where z and y are normalized by W and H, respectively. The dimensionless time t^* is defined as $t^* = (tU_\infty)/H$. The wake exhibits horizontal bimodal switching in a random manner, with the simulation over 2000 convective time units capturing four switches of the wake. The wake is approximately symmetric in the vertical direction, its slight asymmetry caused by the jet generated by the underbody flow. The most probable asymmetric positions of the wake correspond to a horizontal gradient of pressure coefficient of ± 0.20, similar to the values obtained numerically for the same Re_H but using a different code [18]. The maximum time maintained by the wake in one asymmetric position is 750 normalized time units, with an average switch duration being 25 normalized time units. The time-averaged drag coefficient is 0.36, which matches values reported in the literature [29,30,44]. The length of the recirculation bubble is $\overline{L_R} = 1.42H$, defined based on the time-averaged streamwise velocity, and the time-averaged pressure coefficient $\overline{C_{\mathrm{Pbase}}} = -0.22$, consistent with the experimental results of Grandemange *et al.* [16] and the LES results of Hesse

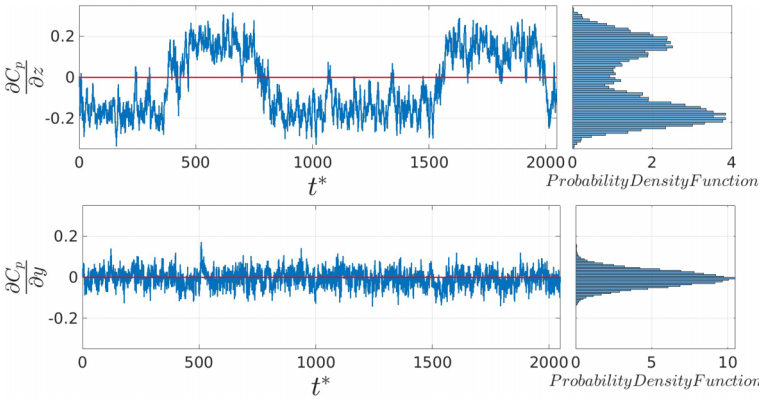

FIG. 6. Time evolution of the horizontal (top) and vertical (bottom) gradients of pressure coefficient on the base and the associated probability density functions.

and Morgans [30]. The time-averaged pressure coefficient during the switching, when the wake is instantaneously symmetric, is -0.21 compared to -0.232 for the asymmetric wake states.

A toroidal vortex ring structure is formed in the near-wake region, matching previous studies [8,9,20,45–47]. Horizontal bimodal switching causes the near-wake toroidal structure to tilt towards and away from the base stochastically. During the switching period, the toroidal structure becomes instantaneously parallel to the base, representing a symmetric wake. This effect is projected onto the base pressure as a low-pressure region associated with the vortical structure being locally close to the base. Figure 7 shows this behavior and the associated base pressure for the three cases, when the wake is tilted towards the positive z direction, during switching when the wake is instantaneously symmetric and after the switching when it is tilted towards the negative z direction. These results

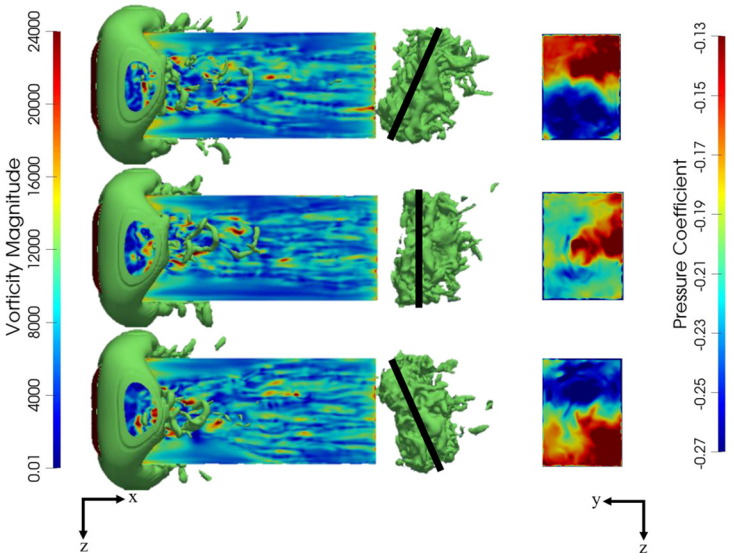

FIG. 7. Left: Isocontours of the coefficient of pressure $C_P = -0.2$, as well as the vorticity distribution on the body top surface, indicating the near-wake vortical structures for different wake positions. Right: The associated C_p on the base.

are consistent with previous experimental [12] and numerical results [18] which capture side-to-side bimodality.

IV. BIMODALITY MODEL

The present work adopts a nonlinear feedback control approach in order to target suppression of the bimodal switching, which is itself a nonlinear phenomenon. The controller will be based upon a stochastic model in the form of a nonlinear Langevin equation, which captures the evolution of the reflectional symmetry breaking in the turbulent wake of the Ahmed body. This model was initially developed to characterize the random symmetry-breaking behavior in the turbulent wake of an axisymmetric body, this exhibiting multimodal behavior [15]. It is based on the premise that multimodality occurs due to the persistence of the laminar global modes at high Reynolds number, with the turbulent fluctuations acting to push stochastically between asymmetric stable positions. The deterministic part (the drift) of the Langevin model captures the nonlinear dynamics of the reflectional symmetry breaking in the laminar flow regime, employing the typical Landau equation. The stochastic part represents the effect of turbulent fluctuations:

$$r(t)t = -\lambda r^3 + \alpha r + \sigma\zeta(t). \tag{7}$$

Brackston *et al.* [21] adapted the model for rectilinear bodies exhibiting bimodality, such as the square-back Ahmed body. Barros *et al.* [24] employed a coupled Langevin model to represent the transition of the wake form the vertical asymmetric state to a horizontal bimodal with vertical symmetry. The adapted Langevin model is shown in Eq. (7). The parameter r is some measure of the modal amplitude, α is the growth rate, and λ the saturation parameter. The first two terms on the right-hand side represent the spatial symmetry-breaking mode, which arises due to a supercritical pitchfork bifurcation at laminar Reynolds numbers, as described in Sec. I. The last term represents the turbulent broadband forcing acting on the coherent structures of this mode, with $\zeta(t)$ a random dynamics of a standard Wiener process and σ^2 the noise intensity; it is expected to capture all flow disturbances that cause wake switching between the two asymmetric states.

The parameter chosen to characterize the wake mode position, $r(t)$, is the center of pressure on the base, calculated as shown in Eq. (8), where $P(x, y, z, t)$ is the pressure and W the width of the base and A_{base} is the base area. A value of $r(t) = 0$ corresponds to a symmetric wake. According to the model, $r(t)$, moves within closed bounds around one of the two asymmetric states until sufficiently perturbed by the stochastic term to switch to the other. The corresponding probability density function of $r(t)$, obtained experimentally at different Re, shows little dependence on Re in the turbulent regime [21]:

$$r(t) = \frac{1}{W\iint_{A_{\text{base}}} P(x, y, z, t)\, dA} \iint_{A_{\text{base}}} zP(x, y, z, t)\, dA. \tag{8}$$

The model parameters for the current Ahmed body, (α,λ,σ^2), were identified by fitting the model to the unforced flow data. The time-averaged mean square displacement (MSD) of the center of pressure, $r(t)$, is shown in Fig. 8(a). Its value is calculated as $\langle[r(t + \delta t) - r(t)]^2\rangle$, where δt here has the same value as the simulation time step. The findings are consistent with those of Rigas *et al.* [15]: the MSD is found to be proportional to the lag time, δt, before starting to plateau. A linear least-square fit was used to estimate the value of the noise intensity for the short timescale region, where $\langle(\Delta r(\delta t))^2\rangle = 2\sigma^2 \times \delta t$. The value of the noise intensity is found to be $\sigma^2 = 0.64$. The probability density function (PDF) of the model, obtained using the steady-state Fokker Plank equation [Eq. (9), where C represents a normalizing constant], was matched to the probability density function of $r(t)$ from the unforced simulation [Fig. 8(b)]. This allowed estimates of both α and λ to be obtained as 3.6 and 91.0, respectively. With reference to Barros *et al.* [24], the values of these parameters are

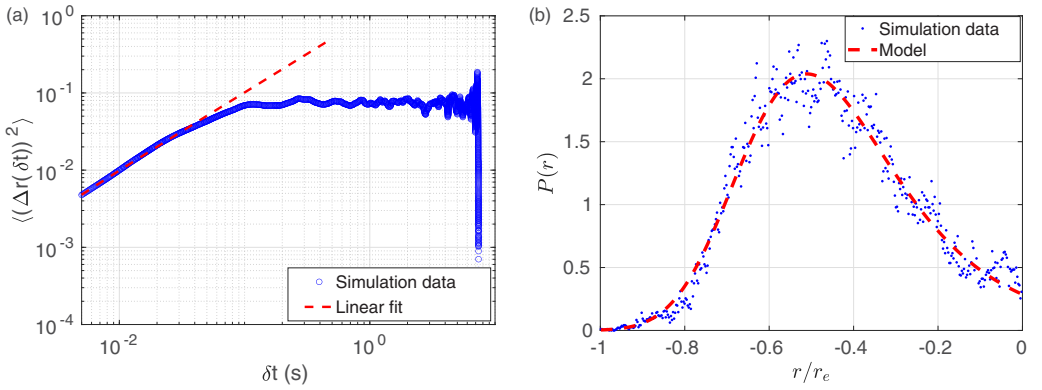

FIG. 8. (a) Mean square displacement (MSD) of the center of pressure $r(t)$ in the unforced case (blue) and a linear fit (red dashed line) to estimate the noise intensity σ^2. (b) Probability density function of the model (dashed red line) and the data of one asymmetric stable position of the wake (blue dots).

for a weakly vertically asymmetric wake, as identified for the unforced case:

$$P(r) = C \exp\left(\frac{\alpha}{\sigma^2} r^2 - \frac{1}{2}\frac{\lambda}{\sigma^2} r^4\right). \tag{9}$$

V. FEEDBACK CONTROL DESIGN

Due to the strongly nonlinear behavior underpinning the bimodal switching [15], we seek to develop a nonlinear feedback controller based upon the above Langevin model. The sensor signal, $r(t)$, which acts as the input signal to the controller, is a measure of the horizontal center of pressure on the base. $r(t)$ is calculated by placing *48* sensors on the base of the Ahmed body at a horizontal normalized distance of $\Delta z = 0.125$ between each successive sensors and a vertical normalized distance of $\Delta y = 0.17$. The output signal from the controller is then fed to the synthetic jet actuators, which are located in a gap around the outer perimeter of the base with a width of $0.04H$. The jet actuation is purely in the streamwise i.e., x direction. It is horizontally antisymmetric, such that the actuation on the right is in antiphase with the actuation on the left as shown in Fig. 1. At any instant in time, the actuation has zero net mass flux, since the left and right mass injection cancels: streamwise momentum is sucked from one side of the base and blown through the other. Thus a single signal dictates the spatial variation around the whole actuation perimeter. The block diagram of the single-input single-output feedback control is shown in Fig. 9.

Based on this system, a Lyapunov function based nonlinear controller was synthesized. The application of this technique for controlling nonlinear systems was introduced by Artstein [48], who established a link between the continuous stabilization of a nonlinear system and the existence of a control Lyapunov function. In this study, a quadratic Lyapunov function is used, as defined

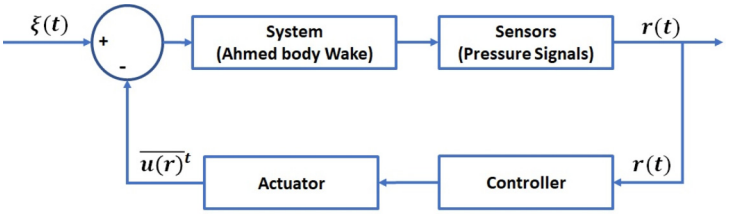

FIG. 9. Block diagram of the feedback control loop.

through Eq. (10). $V(r)$ is a positive definite function which is continuously differentiable and decreases with time, i.e., $V(r) > 0, \forall \mid r \mid > 0$ and $V(0) = 0$. The negative definite derivative of the Lyapunov function, shown in Eq. (11), guarantees the asymptotic stability of the closed-loop controlled system for the given range of r that corresponds to the position of the asymmetric wake in the unforced case [49]. The control law is represented by Eq. (12), where $u(r)$ is the controller signal sent to the actuator, A and B are time-independent amplification factors and λ and α are the model parameters estimated from the unforced case results in Sec. IV. The controller signal $u(r)$ represents the nondimensional actuator jet velocity, i.e., $u(r) = U_{\text{jet}}(t)/U_\infty$. The robustness of the controlled system to variations in the controller parameters was was examined. The controller was found to be asymptotically stable for $0 < (\alpha, \lambda) \leqslant \infty$. The amplification parameter B, must be a positive value to maintain the asymptotic stability of the controlled system. A represents a scaling parameter of the controlled signal:

$$V(r) = \tfrac{1}{2} r^2, \tag{10}$$

$$\frac{dV}{dt} = \frac{dV}{dr} \times [\dot{r} + u(r)], \quad \dot{V} < 0, \quad \dot{V}(0) = 0, \quad \forall \mid r \mid > 0, \tag{11}$$

$$u(r) = -A[-\lambda r^3 + (B + \alpha) r]. \tag{12}$$

This feedback control algorithm was implemented in the LES using the SWAK4FOAM (SWiss Army Knife for Foam) library for OpenFoam [43]. The value of the center of pressure, r, is calculated in real time at the relevant simulation time step and fed to the controller. The inherent nonlinearities of the flow necessitate a response time of the wake flow. This is accounted for by employing the weighted moving average of $u(r)$, denoted $\overline{u(r)}^t$ and shown in Eq. (13) where β is a weighting coefficient given by the ratio of the simulation time step (Δt) to a characteristic time equivalent to $\text{St}_H \sim 2$, taken to be the maximum frequency resolved in the unforced flow. Applying the weighted moving average limits the unsteadiness introduced to the streamwise momentum in the wake, which contributes to the drag [50]:

$$\overline{u(r)}^t = \beta u(r)^t + (1 - \beta)\overline{u(r)}^{t-\Delta t}. \tag{13}$$

VI. FEEDBACK CONTROL IMPLEMENTATION

The feedback controller is implemented in simulations, initially with controller parameters $A = 10$ and $B = 60$. The simulation shown in Fig. 10 initially has control switched off, during which time the wake switches once in the horizontal direction. The controller is switched on at $t^* = 640$, with the convective time for the controlled duration of the simulation being 1230. This is significantly greater than the maximum residence time of the wake in a given asymmetric state the unforced case ($t^* = 750$) and is thus deemed statistically sufficient for investigating the controller performance. The effect of the feedback controller are explored in the following subsections, assessing first its effect on the main control objective—suppressing the wake bimodal switching—as well as its effect on the mean flow properties, the mean body drag and the other dynamical wake modes.

A. Bimodality suppression

The main control objective is to suppress the stochastic switching of the wake, as characterized by the horizontal base pressure gradient. The effect of the controller on both the horizontal and vertical pressure gradients is shown in Fig. 10. It is evident that the wake switching behavior in the horizontal direction is completely suppressed. The probability density function of the horizontal base pressure gradient ($\partial C_P/\partial z$) exhibits just a single peak around the center in the presence of control.

Although the controller was designed to target the deterministic part of the bimodality model—the static RSB modes—as discussed in Sec. IV, it also affects the wake oscillations around the

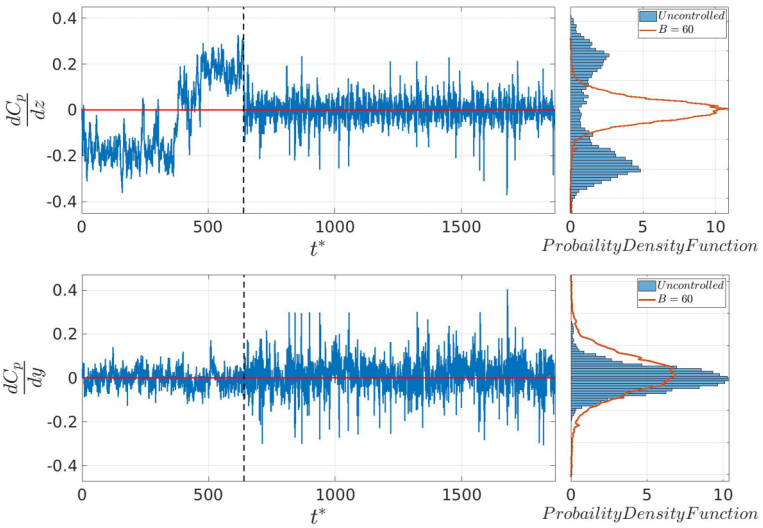

FIG. 10. Horizontal (top) and vertical (bottom) gradients of the coefficient of pressure C_P (left) before and after switching the controller on (black dashed line). The corresponding probability density functions (PDFs) (right) for the uncontrolled case (blue bars) and the controlled case (orange line). the controller parameters A and B are 10 and 60, respectively.

main wake position. These oscillations, which we will term "residual oscillations," are caused by the turbulent disturbances modeled via the stochastic term in the absence of control in Eq. (7). A reduction in the level of these residual oscillations—in the horizontal direction—is achieved after switching the controller on. Thus an advantage of the nonlinear controller is that it results in much reduced maximum horizontal wake offset positions. In the presence of control, the maximum offset wake position corresponds to a horizontal pressure gradient of $\sim \pm 0.08$, which is a 72% reduction in the uncontrolled value of ± 0.29. This is partly due to the wake symmetrization and partly due to the reduced amplitude of the residual oscillations.

Thus, the effect of the controller extends beyond reorienting the asymmetric wake to also alter the higher frequency wake dynamics. These residual oscillations are linked to interactions between the lateral shear layers and the asymmetric wake, consistent with the switching mechanism recently proposed by Haffner *et al.* [22], and may also be partially related to the disturbances convected from the upstream boundary layer dynamics. The degree of reduction in the residual oscillations depends on the ratio between the nonlinear and linear terms of the control law, as it will further be discussed in Sec. VII. The amplitude of the residual oscillations value can be quantified by the root mean square of the trajectory of r_{RMS} at any main position of the wake [Eq. (14), where N is the number of data points of the controlled convective time]. The feedback controller reduces the amplitude of the horizontal residual oscillations by up to 20% compared to the unforced case. The wake then exhibits regular time-periodic behavior with a distinguishable frequency, $\mathrm{St}_{\mathrm{control}}$. Similar time periodic behavior has been observed after implementation of other control strategies, as in case of the opposition control by Li *et al.* [34] and the adaptive control by Varon *et al.* [51]. It is notable that the residual wake oscillations are not only reduced compared to the unforced case, they are also much smaller than has been observed so far after application of linear controllers [21,34]. For the latter, the amplitude of residual oscillations of the symmetrized wake matched the original asymmetric extremes of the wake, two orders of magnitude larger than for the unforced flow. This suggests that the underpinning nonlinear dynamics of the wake, when neglected, amplify the wake residual oscillations in the bimodality direction.

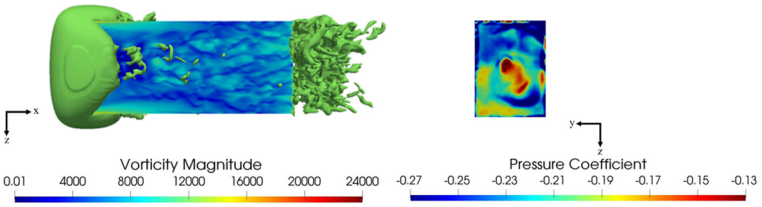

FIG. 11. Isocontours of the coefficient of pressure $C_P = -0.2$ (left) and vorticity distribution on the body surface, indicating the effect of the feedback controller on the near-wake vortical structures, with the associated C_p projected on the base (right).

In the orthogonal (vertical) direction, the controller is observed to have a negligible effect on the mean wake position, but to slightly amplify the vertical residual oscillations, as shown in Fig. 10 ($\partial C_P/\partial y$):

$$r_{\mathrm{RMS}} = \left[\frac{1}{N}\sum_{i=0}^{N} {r_i}^2\right]^{1/2}. \tag{14}$$

B. Mean flow properties and wake topology

This section will explore the effect of the controller on the mean flow properties and the near-wake toroidal-vortex structure, for which stochastic bimodal switching resulted in tilt variations for the unforced case. The effect of control is to orientate this toroidal structure parallel to the base, so that it is approximately horizontally symmetric, as shown in Fig. 11. This matches the instantaneous orientation of the wake during a switching event for the unforced case (Fig. 7), with the symmetric state being unstable in the absence of control. The resulting base pressure coefficient exhibits a higher pressure region near the center of the base surrounded by a region of lower pressure, as shown in Fig. 11. The base pressure coefficient here differs to the unforced case of Fig. 7, where it has minima and maxima on the sides of the base for the asymmetric wake, and looks similar to the instantaneous unstable symmetric wake. The time-averaged base pressure coefficient of the controlled wake is $\overline{C_{\mathrm{Pbase}}} = -0.227$, which represents ~2% reduction in the base pressure compared to the asymmetric wake. This value depends on the amplification parameter, B, in the control law [Eq. (12)], which will further be discussed in Sec. VII.

The effect of the controller suggests that exchanging momentum within the wake region directly effects the streamwise position of the toroidal vortex. Comparing the topology of the symmetrized wake to that when a base cavity is used [32], for the latter drag reduction was associated with minimizing the imprint of the toroidal vortex on the base, this being correlated with an increase in the average base pressure. For the present feedback control, the proximity of the toroidal vortex to the base slightly hinders the recovery in average base pressure, which is likely to limit the reduction in pressure drag. The length of the recirculation region for the controlled case is reduced by 8% compared to the unforced case, with a value $\overline{L_{R-\mathrm{cont}}} = 1.32H$. Thus the feedback control reduces the length of the recirculation bubble while also reducing the drag. This differs from findings in the absence of unsteady actuation or feedback control, where shorter recirculation bubbles imply increased drag [52,53], but is consistent with other feedback control studies, where the change in the recirculation length was more related to actuation location than drag reduction [54]. Figure 12 shows the streamlines on a horizontal plane at the midheight of the body. The unforced streamlines indicate the tilt of the toroidal vortex via a skewness of the vortex centers, while the controller restores the alignment of these centers, shortens the bubble length, and increases the streamlines curvature.

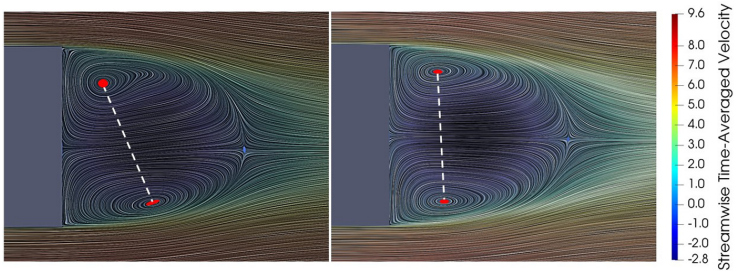

FIG. 12. Streamlines based on the time-averaged streamwise velocity projected on a plane at midheight of the body. The unforced case is shown on the left and the controlled case ($B = 60$) is shown on the right.

C. Ahmed body drag

As mentioned in Sec. I, previous studies have suggested that a symmetric wake corresponds to ∼9% base pressure recovery [16,22]. This was estimated based on comparing the average base pressure during switching events, when the wake is instantaneously symmetric, to its value while the wake is asymmetric. This suggests potential for reducing the pressure drag by suppressing wake bimodality.

The current results confirm that resymmetrizing the wake using nonlinear feedback control increases the average base pressure and reduces the pressure drag. The time-averaged drag is reduced with higher fluctuations of C_D, as shown in Fig. 13. $\overline{C_D}$ is reduced by 2.5% for the case with the controller parameters $A = 10$ and $B = 60$. Similar to mean flow properties, the percentage of drag reduction has a strong dependence on the value of B, that controls the contribution of the linear terms in the control low. This dependence leads to the parametric study in Sec. VII A. In case of $B = 1$, the time-averaged drag is reduced by 7.4%, which represents the maximum drag reduction achieved using the current nonlinear feedback controller. This reduction is lower than the expected 9%, due to the streamwise position of the toroidal vortex in the near wake. These simulations reveal that the drag reduction achieved by symmetrizing the wake, depends on the way of suppressing wake bimodality and its effect on the mean flow in the wake. To conclude, these results confirms that pressure drag is sensitive to wake bimodality. The application of the nonlinear controller symmetrized the wake by affecting the separated shear layers in the separatix. This effect alters the balance of disturbances in shear layers and the streamwise position of the disturbances, which will be further discussed in Sec. VII C. The level of the disturbances imposed influences the base pressure and accordingly the drag.

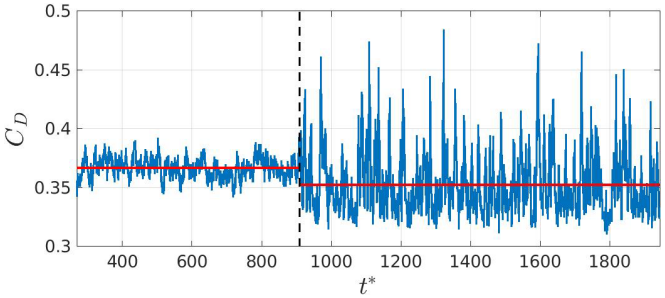

FIG. 13. Effect of feedback control on the drag coefficient (C_D). The controller is switched on at $t^* = 935$ shown with black dashed line. The values of the controller parameters A and B are 10 and 60, respectively. The red line indicates the mean values of C_D prior to and after switching on the controller.

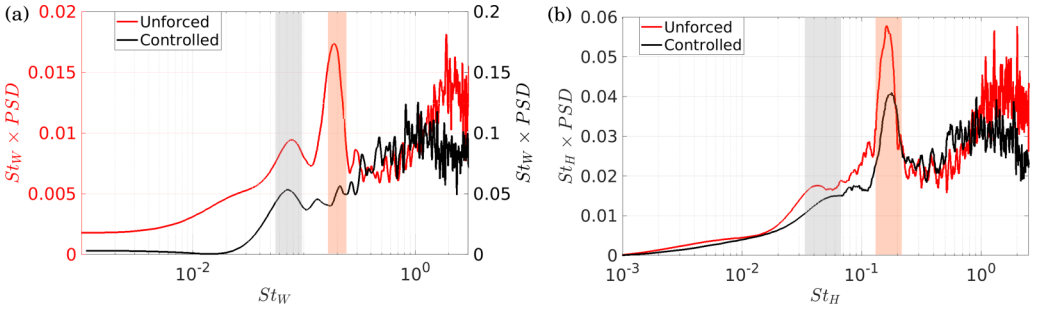

FIG. 14. Premultiplied spectra of the (a) horizontal and (b) vertical antisymmetric base pressure signals for both the unforced (red) and the controlled (black) cases. Gray and red shaded areas indicate the broad frequency band related to the bubble pumping mode and vortex shedding frequency, respectively.

D. Periodic modes in the wake

Here we investigate the effect of the controller on the time-periodic modes in the wake using spectral analysis of the base pressure. The symmetric and antisymmetric base pressure signals considered in the following analysis are defined in Eqs. (15) and (16), respectively, where M is the number of the pressure probes, n_1 and n_2 are the distance of the pressure probes on the base to its center in either of the crossflow directions (y, z) as shown in Fig. 1:

$$\Delta P|_{\text{Symmetric}} = \frac{1}{M}\left[\sum_M P(x,y,z)|_{n_1} + \sum_M P(x,y,z)|_{n_2}\right], \tag{15}$$

$$\Delta P|_{\text{Anti-symmetric}} = \frac{1}{M}\left[\sum_M P(x,y,z)|_{n_1} - \sum_M P(x,y,z)|_{n_2}\right]. \tag{16}$$

Figure 14 shows the effect of the controller on the antisymmetric base pressure spectra in both the horizontal and vertical directions. The normalized frequency, i.e., St number is calculated based on the body length in the direction of the antisymmetric base pressure. The unforced signal in both directions indicates three periodic modes. The first appears with a broadband frequency around $\mathrm{St}_W \sim 0.07$ in the horizontal signal [Fig. 14(a)] and around $\mathrm{St}_H \sim 0.05$ in the vertical signal [Fig. 14(b)], is associated with the streamwise bubble pumping mode. This mode was detected in the base pressure spectrum in experiments by Khalighi *et al.* [55] and has been hypothesized to occur due to a periodic interaction of the top and bottom halves of the toroidal vortex trapped in the near-wake region, causing a periodic change in the recirculation region. A further suggestion relates it to a nonlinear interaction between the vertical and horizontal vortex shedding [20]. Although a linear stability analysis of the wake behind an axisymmetric body has not captured this mode [56], it has been detected in spectral analysis of the wakes of an axisymmetric body [5], a circular disk, and a sphere wake [57]. The second mode is associated with a peak at $\mathrm{St}_W = 0.19$ in the horizontal direction [Fig. 14(a)] and $\mathrm{St}_H = 0.17$ in the vertical direction [Fig. 14(b)] and relates to vortex shedding in both directions. The same frequencies were reported in experimental studies by Volpe *et al.* [20] and Lahaye *et al.* [58]. The vortex shedding frequencies in both directions are consistent with the range of frequencies reported in the literature of 0.13–0.19 [11,29,59]. The third dynamical mode, for the unforced base pressure, appears in Fig. 14 at $\mathrm{St}_W \sim 1.9$ and $\mathrm{St}_H \sim 1.6$ and is linked to the higher frequency dynamics of the shear layers in both directions.

The base pressure spectra, horizontally and vertically antisymmetric, are shown in the presence of feedback control in Figs. 14(a) and 14(b), respectively. Both signals capture the same periodic modes evidenced in absence of the controller. In the horizontal direction, the controller amplifies the energy content of all these modes. The horizontally antisymmetric base pressure signal [Fig. 14(a)], captures the symmetric bubble pumping mode at the same frequency of the unforced case. Unlike

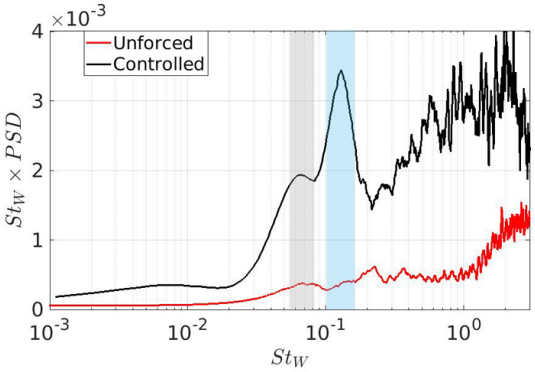

FIG. 15. Symmetric premultiplied base pressure signals for both unforced (red) and controlled (black) cases. Gray and blue shaded areas indicate the broad frequency band related to the bubble pumping mode and the frequency associated with the streamwise motion of the toroidal vortex, respectively.

for the unforced case, the controlled signal does not capture a clear peak for the horizontal vortex shedding. A relatively smaller peak around $\mathrm{St}_W = 0.2$ is seen, this suggesting that the antiphase low-frequency forcing of the controller disturbs the dynamics of the horizontal vortex shedding. This will be further discussed using the POD analysis in Sec. VIII. The energy content of the free shear layers is increased by an order of magnitude in the presence of the feedback controller, with a relatively lower frequency of $\mathrm{St}_W \sim 1$ compared to the unforced case ($\mathrm{St}_W \sim 1.9$). Similarly, the vertically antisymmetric spectrum [Fig. 14(b)] shows how the controller slightly reduces the energy content of these three modes. The energy content of the vertical vortex shedding mode is reduced with a slight increase in the associated frequency from $\mathrm{St}_H = 0.17$ without control to $\mathrm{St}_H = 0.19$ with control. This shift in the vortex shedding frequency is consistent with the recent experimental results by Plumejeau *et al.* [23], which concluded that the symmetric wake configuration is associated with a higher shedding frequency in both cross-flow directions. The vertically antisymmetric signal captures the shear layer dynamics at a frequency equivalent to $\mathrm{St}_H \sim 1$, this frequency having shifted downwards compared to the uncontrolled case ($\mathrm{St}_H \sim 1.6$).

The unforced symmetric base pressure signal, shown in Fig. 15, captures a broad frequency band around $\mathrm{St}_W \sim 0.07$ related the bubble pumping and high-frequency shear layers dynamics at $\mathrm{St}_W \sim 2.4$. The controller increases the energy content of the whole spectrum without changing the bubble pumping frequency. A clear frequency peak at $\mathrm{St}_W \sim 1.3$ is evidenced in the presence of the feedback controller. This is attributed to a new symmetric behavior linked to the effect of the momentum exchanged in the wake after control has been switched on. The new symmetric behavior associated with frequencies of $\mathrm{St}_W = 0.13$ ($\mathrm{St}_H = 0.1$ in the vertical direction) is found to be related to streamwise motion of the near-wake toroidal vortex structure after it has symmetrized. Figure 16 shows the time evolution of the of the steamwise position of the toroidal vortex represented by the pressure coefficient isosurface. The time interval between each successive snapshot is equivalent to $\mathrm{St}_W = 0.13$. In symmetrizing the wake, the controller causing a transitional motion of this toroidal vortex. Dynamics of the shear layers are also captured in the controlled signal with an associated frequency of $\mathrm{St}_W \sim 2$.

The effect of the controller on the dynamical modes in the wake can be concluded as follows; the low-frequency bubble pumping mode is largely unaffected by suppressing the horizontal bimodal switching and by the reduction in the high-frequency horizontal residual oscillations. The vertical vortex shedding frequency increases due to the action of control. The horizontal vortex shedding, however, has not been clearly evidenced, as the interaction of the horizontal shear layers is now disturbed by the controller. The different effects of the controller on the vortex shedding mode in the horizontal and vertical directions is attributed to the setup of the actuation slots, shown in

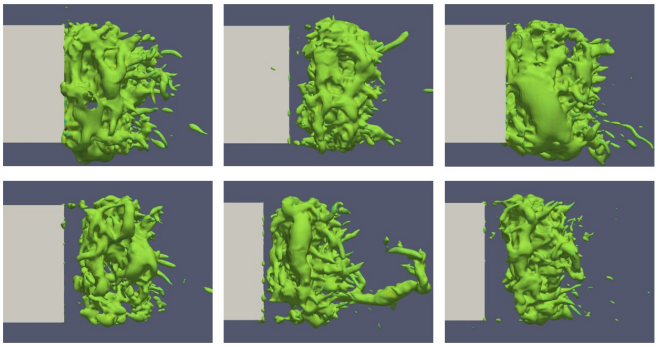

FIG. 16. Instantaneous snapshots of the near-wake toroidal vortex indicated by the isocontours of the pressure coefficient ($C_P = -0.2$). It indicates the time evolution of the streamwise location of the toroidal vortex with a time interval corresponding to $\mathrm{St}_W = 0.13$ between each successive snapshots starting on the top left to the bottom right.

Fig. 1. The horizontal shear layers are subjected to antiphase forcing, while the vertical shear layers are forced in-phase. The stochastic horizontal switching of the wake is replaced by an oscillatory motion of the toroidal vortex structure in the streamwise direction, due to exchanging momentum between the lateral sides of the wake. Finally, the spectral analysis of the antisymmetric controlled signals indicates an increased energy level relative to the unforced case in the horizontal direction, while in the vertical direction the energy has decreased.

VII. NONLINEARITY AND BIMODALITY SUPPRESSION

As mentioned in Sec. VI, the performance of the feedback controller depends on the choice of controller parameters in the control law given by Eq. (12). A parametric study of the feedback control law parameters, A and B, is now carried out to investigate the effect on bimodality suppression, drag, and wake dynamics. Parameter A amplifies the control effort and directly affects the wake response time, resulting in a faster wake response for $A > 1$. The threshold value to symmetrize the wake is $A = 10$, yet as A increases, the drag reduction decreases. This is likely to be because larger values of A increase the momentum coefficient and subsequently enhance the near-wake entrainment. This directly affects the shear layers and their associated interactions, amplifying the higher frequency dynamics in the near-wake region. Parameter B represents an amplification factor of the linear term of the control law. A range of $0 < B \leqslant 90$ is investigated for $A = 10$. Exploring the contribution of the linear term offers an insight into the effect of nonlinearity on suppressing bimodality and its associated interactions in the wake. The effect of varying B is discussed in detail in the following subsections.

A. Wake symmetry, wake oscillations, and body drag

The effect of varying B on the wake symmetry, residual oscillations, base pressure, and drag reduction is first explored. The effect of varying B on the degree of wake symmetry, which is characterized by the value of the horizontal gradient of the base pressure coefficient, $\partial C_p/\partial z$, is shown in Fig. 17(a), with a more symmetric wake associated with lower values of $\partial C_p/\partial z$. It can be seen that the level of wake symmetry increases with B. For $0 < B < 10$, the same order of magnitude as the growth rate α, fluctuations in $\partial C_p/\partial z$ show a maximum reduction of 25% compared to the unforced case, and the wake exhibits little sensitivity to B. When B is one order of magnitude higher than α, i.e., $B > 10$, the wake symmetry starts to increase with B, the maximum reduction in wake asymmetry being reached at $B = 90$, beyond which no further reduction is achieved. The value of $\partial C_p/\partial z$ is then reduced by 72% compared to the unforced case and the wake can be considered

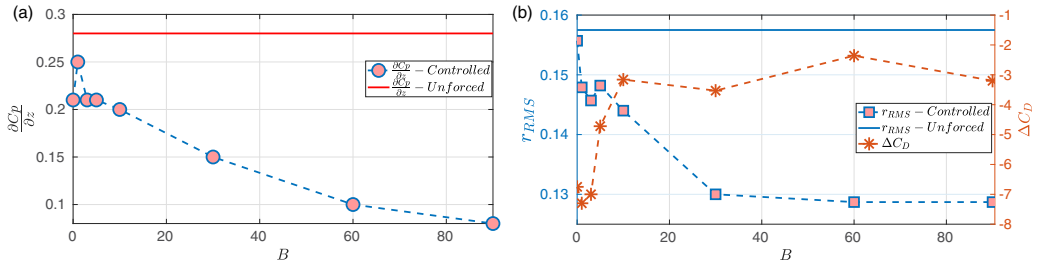

FIG. 17. (a) The variation of the horizontal gradient of the base pressure coefficient (used to indicate the level of wake symmetry) with the controller parameter B. The red line indicates the value of $\partial C_p/\partial z$ for the unforced case. (b) The blue dashed line is the root mean square (RMS) of the instantaneous center of pressure for different values of the controller parameter, B. The blue solid line shows the RMS value for the uncontrolled case. The orange line is the variation in drag reduction with B.

symmetrized in this region. In this case (i.e., $B = 90$), the linear term dominates the control effort, with B almost two orders of magnitude higher than α. Relating the value of the linear term parameter, B, to the growth rate parameter, α, suggests that the growth of the mode r could be suppressed with a linear controller.

The residual wake oscillations around the mean wake position, characterized by the root mean square of r, r_{RMS}, are also affected by the tuning of B. As shown in Fig. 17(b), r_{RMS} exhibits a decreasing trend as B increases, reaching a minimum when $B = 60$, without further reduction for higher values of B. This confirms a significant benefit of the present nonlinear controller over the linear controllers employed in previous studies. There, control led to amplification of the horizontal residual oscillations, and this was linked to low values of drag reduction of less than $\sim$2% [21,34,35]. Figure 17(b) also depicts the variation of the drag reduction as B varied. For the present results, low levels of horizontal residual oscillations do not seemed to be directly linked to drag reduction; when the residual oscillations are small, the mean drag reduction is also small. The maximum drag reduction achieved by feedback control is 7.4%, a significant increase on the 2% reported previously using a linear controller. For this maximum reduction, $B = 1$ (hence $0 < B \leqslant \alpha$), which means that the nonlinear term dominates the control effort, the wake then oscillates at a frequency of $\mathrm{St}_{\mathrm{control}} = 0.024$.

The drag reduction decreases as B increases and hence the contribution of the linear controller term increases. A minimum drag reduction of 2.5% occurs for a fully symmetrized wake; the residual fluctuations of the wake are also smallest. Comparing Figs. 17(a) and 17(b), a trade-off between drag reduction and wake symmetry is evident, suggesting that drag reduction is not directly related to symmetrizing the wake, but linked to suppression of the nonlinear interactions between the stochastic bimodality and other periodic modes in the wake. A favorable manipulation of these nonlinear interactions is attained when the nonlinear term of the controller dominates the control effort (i.e., $B \leqslant \alpha$), suggesting the need for a nonlinear controller in order to reduce the drag.

Table II shows the change in the mean flow properties as B varies. The time-averaged base pressure coefficient, $\overline{C_{\mathrm{Pbase}}}$, decreases with B, inhibiting the reduction in pressure drag. A linear relation between $\overline{C_{\mathrm{Pbase}}}$ and $-\Delta\overline{C_D}\%$ can be seen here, confirming the dominant effect of the base pressure on pressure drag [4]. For all values of B, some base pressure recovery is evidenced compared to the unforced case. The maximum average increase in the base pressure was less than the 9% indicated in the literature. This is suggested to be a result of the controller shifting the near-wake toroidal vortex closer to the base, limiting the base pressure recovery. The minimum value of $\overline{C_{\mathrm{Pbase}}}$ occurs for $B = 60$, and is associated with the least drag reduction. This case achieves a relatively high level of wake symmetry, with the linear control term dominating the control effort. The length of the recirculation bubble, $\overline{L_R}$, is reduced in presence of the feedback control for all values of B compared to the unforced case. This length also decreases as B increases. A reduction of 3.5%

TABLE II. Effect of changing the amplification parameter B on the mean flow parameters; the time-averaged base pressure coefficient ($\overline{C_{\mathrm{Pbase}}}$), recirculation bubble length ($\overline{L_R}$), average drag reduction ($\Delta\overline{C_D}$), and control effort characterized by the momentum coefficient ($\overline{C_\mu}$) and the resultant frequency of the periodic switching in the wake ($\mathrm{St}_{\mathrm{control}}$).

B	$\overline{C_{\mathrm{Pbase}}}$	$\frac{\overline{L_R}}{H}$	$-\Delta\overline{C_D}\%$	$\overline{C_\mu} \times 10^3$	$\mathrm{St}_{\mathrm{control}}$
Unforced (Asymmetric wake)	−0.232	1.44	0.00	0.0	0
0.01	−0.209	1.36	6.75	1.2	0.021
1	−0.207	1.38	7.40	1.2	0.024
3	−0.208	1.37	7.00	1.2	0.025
5	−0.214	1.34	4.72	2.0	0.033
10	−0.217	1.33	3.16	3.0	0.034
30	−0.216	1.34	3.53	3.3	0.040
60	−0.218	1.32	2.50	3.9	0.054
90	−0.217	1.33	3.20	3.9	0.050

in $\overline{L_R}$ is reported for the case of maximum drag reduction ($B = 1$) compared to the asymmetric unforced wake, while a 9% reduction in $\overline{L_R}$ is reported for the minimum drag reduction. Comparing the controlled cases, it can be seen that a longer bubble allows for higher base pressure recovery and consequently reduced drag [21,32]. However, we suggest that the underlying mechanism of drag reduction achieved here is not limited to the bubble length but is also influenced by the suppression of wake symmetry breaking.

B. Control performance

The effect of tuning B can also be characterized using the barycenter of pressure, $r(t)$, i.e., the controller input defined in Eq. (8). The maximum deviation of the wake from the center of the base in the absence of control corresponds to $r = \pm 0.32$, which represents the switching bounds of the unforced wake. The contribution of the controller nonlinear term was assessed for different values of B. For $B = 0.01$, the controller is linear when the spatial position of the wake lies in the space $-0.05 \leqslant r \leqslant 0.05$. That is, the contribution of the nonlinear part of the controller is negligible when the wake is close to being symmetric. The contribution of the controller nonlinearity then increases as the wake deviates from the linearly dominated region. The range of r for which $u(r)$ is almost linear increases with B, implying a larger linearly dominated region for higher values of B. For $B = 90$, the linearly dominated region extends to $-0.14 \leqslant r \leqslant 0.14$, beyond which, the contribution of the nonlinear term in the control effort does not exceed 10%. This suggests the possibility of suppressing wake bimodality using purely linear controllers, even though the nonlinearity inherent in the interactions of this mode with the other dynamical modes and the effect on drag reduction remain open questions.

Figure 18 shows the time history of the controller input, $r(t)$, and the output, $u(r)$. Both signals are periodic with a frequency corresponding to $\mathrm{St}_{\mathrm{control}} = 0.024$ for $B = 1$, the case where maximum drag reduction is achieved. The time delay between the signals is related to the wake response time to actuation. The value of $\mathrm{St}_{\mathrm{control}}$, which is associated with the wake oscillations that occur in the presence of feedback control, increases as B increases. For B in the range $0 < B \leqslant 90$, the frequency lies in the range $0.02 < \mathrm{St}_{\mathrm{control}} < 0.054$, as indicated in Table II. The drag reduction decreases as $\mathrm{St}_{\mathrm{control}}$ becomes closer to the bubble pumping frequency. The interaction between the periodic switching and the bubble pumping modes is seen to limit the drag reduction. Comparing the sensor signal, $r(t)$, for the controlled and uncontrolled cases, Fig. 19 indicates a cutoff frequency, $\mathrm{St}_{\mathrm{cutoff}}$, where the action of control starts to amplify rather than attenuate oscillations. Dynamical modes below $\mathrm{St}_{\mathrm{cutoff}}$ are attenuated, by the action of the control, while those above are amplified. Across

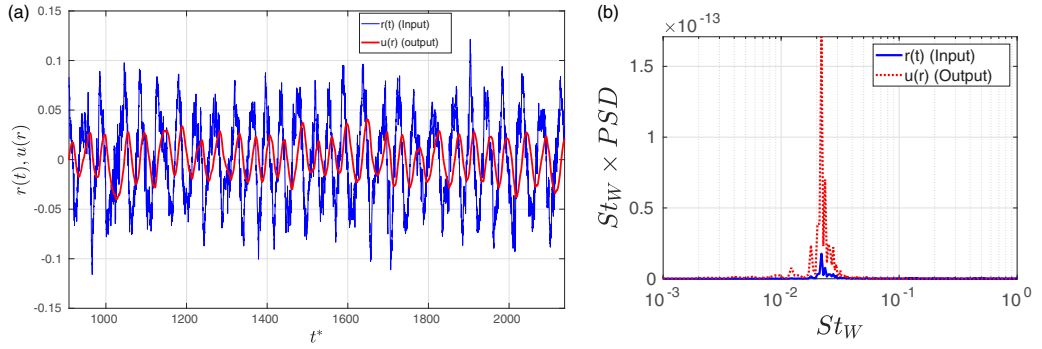

FIG. 18. (a) Time evolution of the input and output signals of the nonlinear controller for the case of $B = 1$. The associated frequency of both signals corresponds to $\mathrm{St}_{\mathrm{control}} = 0.024$.

different controller parameters, $\mathrm{St}_{\mathrm{cutoff}}$ has a similar order of magnitude to the peak bimodality frequency, its value increasing as B increases, reaching a maximum value of $\mathrm{St}_{\mathrm{cutoff}} = 0.013$ for the case in which the linear control term exceeds the nonlinear term by two orders of magnitude and the wake is fully symmetrized ($B = 90$). Tighter switching bounds of the wake are associated with higher cutoff frequency. This indicates that the model considered here, based on Langevin dynamics, successfully captures the low-frequency dynamics associated with bimodality. If the synthetic jet actuators can be assumed to have an efficiency of $\eta_{\mathrm{actuator}} = 0.95$ (95%), the maximum power utilied by the controller, $Pw_{\mathrm{actuation}}$ would not exceed 0.5% of the total power saved due to drag reduction, Pw_{saved}.

The momentum coefficient of the actuation associated with control, C_μ, increases with B. The maximum C_μ for the case of maximum drag reduction ($B = 1$) was 8.5×10^{-3} with an average value of 1.2×10^{-3} (Table II). As the momentum coefficient increases, the drag reduction decreases, reaching its minimum value when $C_\mu = 7.9 \times 10^{-2}$ with an average of 3.9×10^{-3}. This suggests that higher levels of momentum exchanged in the wake increase the level of turbulent entrainment in the near-wake region, consistent with the description of flow dynamics in the wake by Gerrard [61].

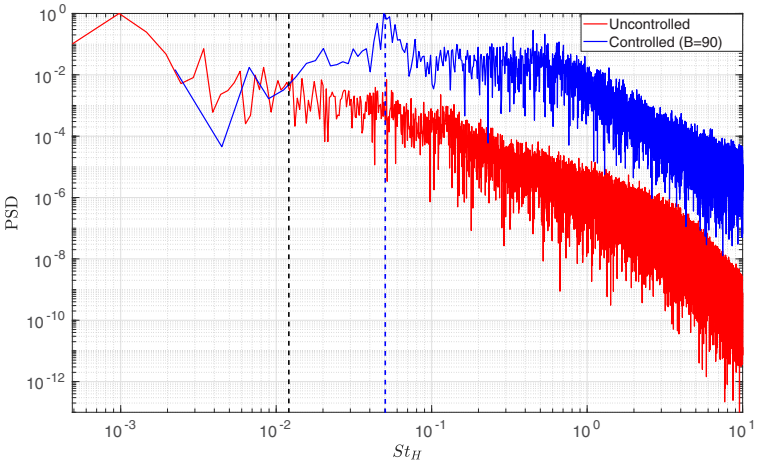

FIG. 19. Power spectral density (PSD) of the uncontrolled (red) and the controlled (blue) center of pressure for the case of $B = 90$, indicating the cutoff frequency $\mathrm{St}_{\mathrm{cutoff}} = 0.013$ (back dashed line) and the frequency peak for the controlled wake $\mathrm{St}_{\mathrm{control}} = 0.05$ (blue dashed line).

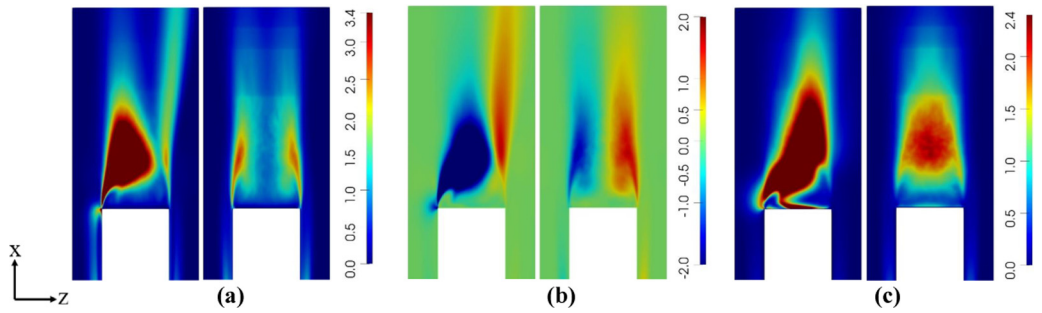

FIG. 20. Time-averaged Reynolds stress components on a central horizontal plane at $y/H = 0.5$. Comparing the uncontrolled asymmetric wake (on the left for each component) and the controlled case (on the right for each component). (a) The streamwise Reynolds stress $\overline{u'_x u'_x}$. (b) The $\overline{u'_x u'_z}$ Reynolds stress. (c) The horizontal (lateral) Reynolds stress $\overline{u'_z u'_z}$.

Increasing C_μ enhances the unsteadiness of the streamwise momentum, which has an unfavorable effect on the drag. The higher levels of momentum exchanged in the wake further increase the disturbances on the free shear layers that have been balanced due to wake reorientation, as discussed previously, which hinders the gain in drag reduction. This suggests that a new control strategy which attenuates the disturbances in the free shear layers might be more effective for reducing the drag.

C. Insights into bimodal switching mechanism

The results suggest that bimodality indirectly affects the drag through the interaction of the asymmetric recirculation region and the shear layers that are shed from the vertical base edges between which switching takes place. Haffner *et al.* [22] recently proposed a mechanism for the wake switching based on flow entrainment related to the lateral shear layer dynamics. Their experimental results suggest that the formation of an asymmetric recirculation region is caused by the large curvature of one shear layer. This curved shear layer triggers the parallel layer downstream of the base, causing a roll-up in the wake which leads to a shedding of a hairpin vortex in the wake [18]. This roll-up creates an engulfed flow that increases the flow entrained into the recirculation region. As this roll-up gets stronger, the triggered shear layer starts to curve forming a new recirculation region opposite to the existing one, leading to a transient symmetric wake. This mechanism is consistent with the present simulations, as shown through the projected streamlines based on the streamwise velocity during the switching event included in the supplementary movie [60]. The drag reduction associated with this transient symmetric wake is related to inhibiting both the trigger of the shear layers and the coherent recirculating motion in the near wake-region [22]. The trigger of the shear layers can be indicated by Reynolds stresses in the wake.

Figure 20 compares the Reynolds stresses on a horizontal plane at the midheight of the body for the asymmetric unforced wake and the controlled wake. An asymmetric pattern is indicated in all three components ($\overline{u'_x u'_x}$, $\overline{u'_x u'_z}$, $\overline{u'_z u'_z}$) for the unforced case. The triggering of the shear layer on the right side of the body ($+z$ direction) is indicated by relatively higher stresses in the streamwise direction ($\overline{u'_x u'_x}$) downstream of the base, while the curved shear layers forming the asymmetric recirculation region exhibit higher levels of both the $\overline{u'_x u'_x}$ and $\overline{u'_x u'_z}$ shear stress components. The spanwise component ($\overline{u'_z u'_z}$) has higher levels towards the triggered shear layer side. For the controlled symmetric wake, the wake exhibits balanced shear stresses on both shear layers.

In the presence of the controller, exchanged momentum through the actuation slots imposes direct disturbances on both shear layers at the separation edges. These disturbances disrupt the switching mechanism discussed above. When the wake resides on one side, the actuation starts to blow air, introducing disturbances on the curved shear layer, while the parallel triggered layer is now

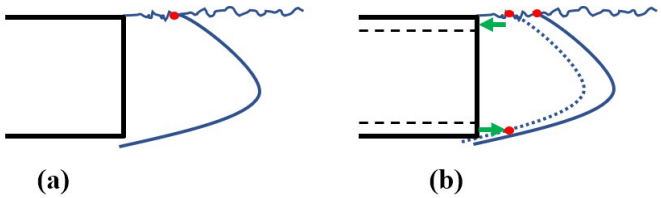

FIG. 21. Schematic description of the effect of the controller on the shear layers in the switching direction. The asymmetric recirculation region formed by the bottom shear layer and its triggering to the top shear layer in the unforced case is shown in (a). The effect of momentum exchange on both shear layers is indicated in (b), where the continuous and dashed lines represent the unforced and the controlled recirculation regions respectively.

subjected to suction by the actuator slot, i.e., shifting the triggering location upstream towards the base and increasing its curvature. The application of the controller with antiphase forcing—blowing on the large curved shear layer and suction on the triggered layer—will have the following effect (Fig. 21):

(1) The blowing on the curved shear layer increases the curvature of this shear layer and accordingly reduces the length of the recirculation region.

(2) This effect forces the triggering location of the parallel layer to take place further upstream, closer to the base.

(3) Applying suction on the other side will have two effects; imposing disturbances on this shear layer closer to the base, promoting earlier growth and promoting the formation of the opposite recirculation region.

(4) When the level of momentum exchanged between the lateral sides and the wake increases, this significantly amplifies the balanced disturbances on the shear layers and accordingly decreases the base pressure (Table II).

Although the application of the controller here inhibits the coherent recirculation in the near wake, which has a favorable effect for drag reduction similar to the symmetric transient state of the unforced case, the disturbances imposed on both shear layers limits the gain in drag reduction. The shear layers disturbances are now balanced, and shifted upstream closer to the base, yielding a more pronounced effect on the base pressure and limiting the drag reduction. The maximum gain in drag reduction is achieved for the case where minimum shear layer disturbances are imposed due to the exchanged momentum. The imposed disturbances on the shear layers amplifies the higher frequency dynamics in the near-wake region, which is confirmed by comparing the power spectral density of r in the absence and presence of control, shown in Fig. 19. Although bimodality is a random behavior of the wake, the unforced flow exhibits a broad peak at $\mathrm{St}_H \sim 10^{-3}$. The effect of control is to amplify the higher wake frequencies, which are associated with $\mathrm{St}_H > \mathrm{St}_{\mathrm{cutoff}}$. We speculate that this amplification creates a coupling between bimodality and the low-frequency bubble pumping mode, consequently driving the random dynamics of bimodality into regular oscillations of the toroidal-vortex within spatial bounds closer to the center. This can be evidenced by the match between the frequency range of the wake oscillations and the bubble pumping frequency. This coupling further causes streamwise oscillations of the toroidal vortex, similar in behavior to the bubble pumping at a frequency of $\mathrm{St}_H = 0.1$, as indicated in Sec. VI D. Thus, the controller changes the stochastic switching of the toroidal vortex into spatially bounded oscillatory switching with streamwise oscillations of this vortex. To conclude, drag reduction is found to be related to the effect of bimodality on the shear layers in the switching direction. Bimodality suppression balances the disturbances in the two parallel shear layers and shifts the streamwise position of the shear layers triggers upstream closer to the base, which found to be unfavorable for base pressure recovery.

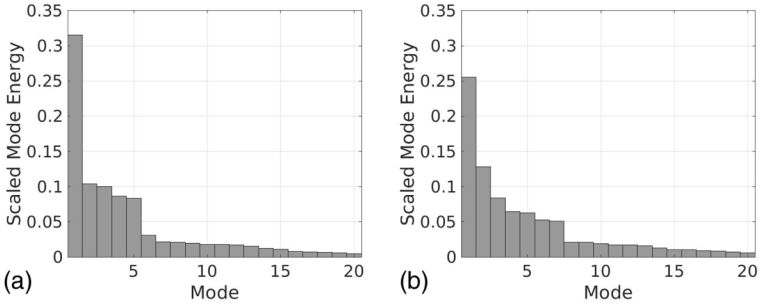

FIG. 22. Energy content of the first 20 pressure POD modes for the unforced (a) and the controlled case for $B = 60$ (b).

VIII. PROPER ORTHOGONAL DECOMPOSITION

In order to obtain more insights into the effect of control on bimodality suppression, proper orthogonal decomposition (POD [62]) of the pressure data on a horizontal plane—parallel to the ground—at midheight of the body is now considered. The total acquisition time was 1000 convective time units, which was deemed sufficient for statistical convergence. The wake residence time within each asymmetric position was equal to that for the unforced case. The sampling frequency corresponded to $\mathrm{St}_W = 2.84$, with $\mathrm{St}_W = fW/U_\infty$, where f is the frequency in Hz. This sampling frequency resolves the highest frequency in the wake.

A. Unforced POD

The energy content of the first 20 modes is shown in Fig. 22. The most energetic first six modes contain ∼73% of the total energy. Reflectional symmetry breaking (RSB) mode, represented by mode 1 in Fig. 23, is the most energetic, with an energy content of 32%, similar to the experimental results by Schmidt *et al.* [35]. This mode is antisymmetric and captures the dynamics of the toroidal vortex structure in the near-wake region, consistent with the recent DNS results by Podvin *et al.* [31]. Spectral analysis of the time coefficient of this mode indicates a broad energy peak at very low frequencies of an order of $\mathrm{St}_W \sim 0.001$. The next four modes capture the dynamics of the frontal separation bubble and the free shear layers in the wake, containing ∼37% of the POD total energy. These modes are associated with the separation and the reattachment of the turbulent boundary layers on the side surfaces of the body. A causal link between the frontal separation bubble dynamics and bimodality was recently suggested by Hesse and Morgans [30]. The power spectral densities of the POD coefficients exhibit peaks at $\mathrm{St}_W \approx 1$–2. The higher frequency $\mathrm{St}_W \sim 2$ is linked to the frontal separation bubble, as it matches the dominant frequency of the pressure signal at the bubble location. The broadband dynamics around $\mathrm{St}_W \sim 1$ are related to shear layer roll-up in the wake, which is suggested to be related to the switching mechanism [22]. Mode 2 and mode 4 have similar structures with a shift in space denoting the convective nature of these modes; the same is true for mode 3 and mode 5. Both mode 4 and mode 5 are not shown for brevity.

Mode 6 in Fig. 23 further shows a mode of combined vortex shedding and bubble pumping. Spectral analysis of the modes' temporal coefficient indicates three peaks at $\mathrm{St}_W = 0.06$, $\mathrm{St}_W = 0.15$, and $\mathrm{St}_W = 0.17$, the first frequency indicating the bubble pumping and the last two associated with the vortex shedding. The time evolution of this combined mode indicates that the energy level varies between the two sides of the wake, depending on the side of the vortex shedding, associated with the asymmetric position of the wake. These results match the POD analysis of the Ahmed body wake using direct numerical simulation by Podvin *et al.* [31].

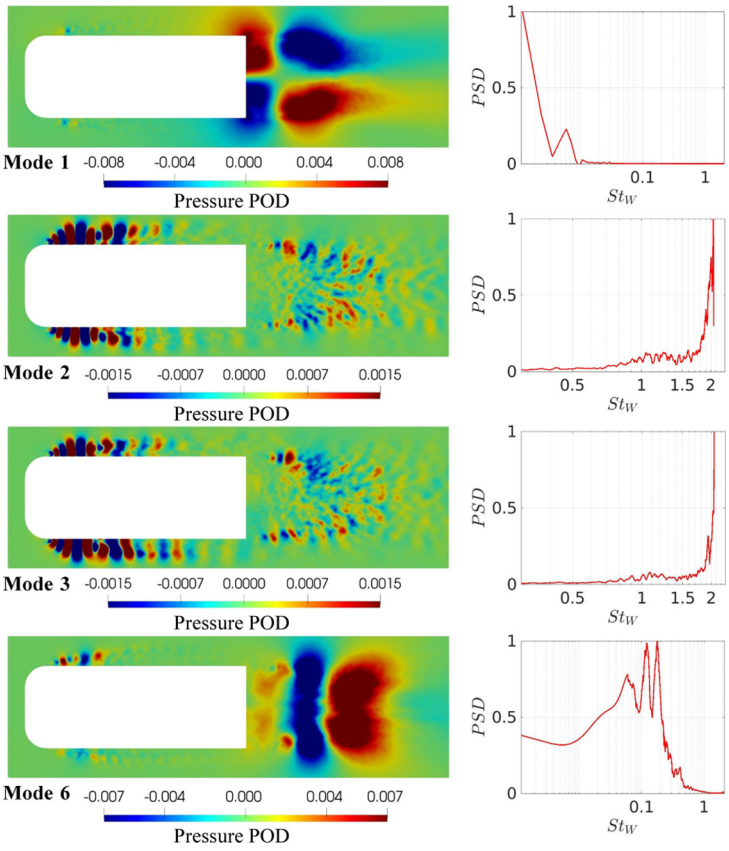

FIG. 23. Pressure POD on a horizontal midplane for the unforced case (left) and their associated power spectral density of their coefficients (right).

B. Controlled POD

The effect of the controller ($B = 60$ case) on the horizontal POD modes is shown in Fig. 24. Similar to the unforced case, the RSB mode, represented by mode 1 in Fig. 24, remains as the most energetic mode, although, its energy content is reduced by 10% compared to the unforced case Fig. 22. It is associated with a frequency of $\mathrm{St}_W = 0.054$, indicating the effect of the controller in replacing the stochastic switching with periodic oscillations. Figure 24 shows that the second POD mode is symmetric and dominated by the streamwise oscillation of the torioidal vortex at a frequency of $\mathrm{St}_W = 0.13$, which was captured previously by the base pressure signal (Fig. 14) and the time-resolved wake topology (Fig. 16). This mode contains 13% of the total energy of the flow and further captures the dynamics of the bubble pumping associated with $\mathrm{St}_W \sim 0.06$ and the shear layer roll-ups at $\mathrm{St}_W \sim 0.5$. Similarly, the third POD mode is symmetric and captures both the streamwise oscillations of the toroidal vortex and the shear layer dynamics represented as a symmetric shedding, and it is not shown for brevity.

Figure 24 shows the fourth mode, which indicates a symmetric shedding of the free shear layers in the wake at a frequency of $\mathrm{St}_W \sim 0.5$. These dynamics were captured by Haffner *et al.* [22] and were suggested to be subharmonics of the shear layer roll-ups occurring downstream of the base (at $x/H \approx 0.3$ from the base) in the unforced case. However, in the presence of the controller, the antiphase forcing exchanges momentum between the lateral sides of the wake, shifting these dynamics upstream closer to the base. Compared to the unforced case, the shedding of each shear

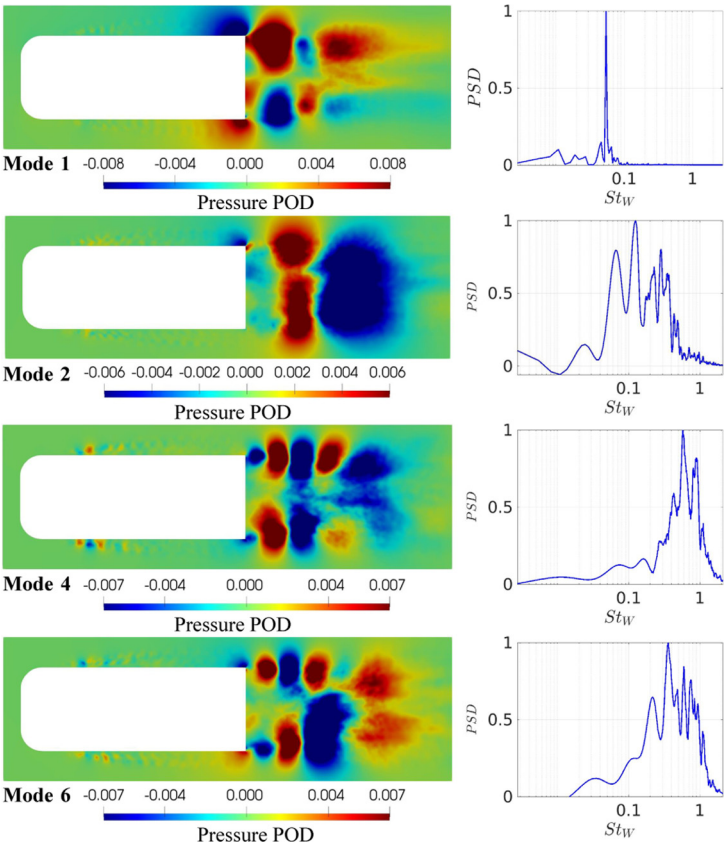

FIG. 24. Pressure POD on a horizontal midplane (left) and the associated power spectral density of their coefficients (right) for the controlled case ($B = 60$).

layer in the controlled case is partially attributed to the actuation, while in the unforced case it was triggered by the interaction with the parallel shear layer. The horizontal vortex shedding is evidenced in antisymmetric mode 6 at $\mathrm{St}_W \sim 0.22$. The energy content of the vortex shedding is doubled compared to the unforced flow. Mode 5 and mode 7 have the same patterns and frequencies as mode 4 and mode 6, respectively, hence are not shown.

The effect of the nonlinear feedback controller on the pressure POD can then be summaried as follows; the energy content of the static RSB mode is reduced and the stochastic switching of the wake is changed to periodic oscillations accompanied by streamwise oscillations of the near-wake toroidal vortex. The energy content of both the horizontal (spanwise) vortex shedding and the free shear layer dynamics are intensified by exchanging momentum in the wake. The increase in the energy level of these modes is expected to limit the drag reduction achieved by wake symmetrization. This increase in the energy content, which is associated with the symmetrization of the toroidal vortex structure, is consistent with the DNS results of Podvin *et al.* [31].

The current controller, despite forcing the locked-in toroidal vortex in the near-wake region, is seen to also significantly affect the separated shear layers affecting other periodic modes in the wake. This confirms the complexity of the interaction between the bimodality and other dynamical modes of the flow. To conclude, the interaction between the wake and the side shear layers can be viewed as an external forcing on the shear layers. This is consistent with the recent experimental study by Haffner *et al.* [22] on the mechanism of bimodality inline with the previous study by Gerrard [61]

on the mechanism of formation of the recirculation region and its relation the entrainment caused by the shear layers in the wake of 2D bodies.

IX. CONCLUSION

The turbulent wake behind a square-back Ahmed body has been investigated using high fidelity wall-resolved large eddy simulations. The simulations successfully captured stochastic bimodal switching from side to side as well as three time-periodic modes in the wake: vortex shedding in both cross-flow directions, roll-up of the free shear layers and a streamwise pumping motion of the recirculation bubble. The latter showed a distinguishable mark on the base pressure, which has not been detected in most previous experimental studies. Bimodality was found to be the most energetic dynamical mode in the wake.

Wake bimodal switching has previously been suppressed with linear control but resulted in large amplitude oscillations of the wake around the center. This study represents a first attempt to employ a nonlinear model-based controller to suppress the bimodal switching. Bimodality is modelled using Langevin dynamics. The controller, derived using a quadratic Lyapunov function, successfully suppresses the bimodal switching. Furthermore, the resulting levels of wake fluctuations are significantly lower than for previous linear controllers. The extent of the fluctuations in asymmetry is significantly reduced. The nonlinear term of the controller is significant when the asymmetric positions of the wake deviates away from the linearly dominated region. The action of control changes the stochastic horizontal switching of the wake to an oscillatory motion of the large coherent structure in the near-wake region, with frequency close to the bubble pumping frequency. The controller does not affect the bubble pumping frequency in the wake, yet leads to stronger and more energetic vortex shedding in both the horizontal and vertical directions.

Changing the relative contributions of the linear and nonlinear terms in the control law significantly changes the wake response. The general trend of driving the stochastic bimodality to time-periodic oscillations holds in all cases, with a trade-off between drag reduction and level of wake asymmetry. A maximum drag reduction of 7.4% is achieved for a semisymmetrized wake, for which the wake switches periodically between asymmetric positions. A fully symmetrized wake with a minimum in residual oscillations around the center of the base corresponds to 2.5% reduction in the drag. Suppressing the wake bimodality using feedback control was shown to reorient the toroidal vortex structure in the near-wake region so that it becomes parallel to the base as well as closer to the base. This consequently disturbs the near-wake shear layers close to the base, limiting the base pressure recovery. It is proposed that this is the main reason that drag reduction is hindered in the case of a fully symmetrized wake. An indirect link between bimodality suppression and drag reduction is shown. Drag reduction is found to be more sensitive to the interaction between the wake bimodal behavior and the shear layers in the switching direction. The effect of this interaction on drag depends on two effects: the unbalanced disturbances imposed on the shear layers and the streamwise position of the disturbances. The latter has a pronounced effect on the base pressure and hence the pressure drag. Controlling this interaction may offer more significant drag reductions, similar to those previously achieved using a base cavity. The current results suggest that control strategies should focus more on suppressing or delaying the interaction between the separated shear layers and the coherent structures in the near-wake region to reduce drag. It also suggests that the actuation position is crucial for suppressing bimodality without amplifying the disturbance on these shear layers.

ACKNOWLEDGMENTS

The authors acknowledge the Islamic Development Banks (IsDB) Ph.D. scholarship for the sponsorship and ARCHER (the UK National Supercomputing service), which was used to run all the simulation cases.

[1] M. N. Sudin, M. A. Abdullah, S. A. Shamsuddin, F. R. Ramli, and M. M. Tahir, Review of research on vehicles aerodynamic drag reduction methods, International Journal of Mechanical and Mechatronics Engineering **14**, 37 (2014).
[2] A. Seifert, O. Stalnov, D. Sperber, G. Arwatz, V. Palei, S. David, I. Dayan, and I. Fono, Large trucks drag reduction using active flow control, in *The Aerodynamics of Heavy Vehicles II: Trucks, Buses, and Trains*, edited by F. Browand, R. McCallen, and J. Ross, Lecture Notes in Applied and Computational Mechanics, Vol. 41 (Springer, Berlin, Heidelberg, 2009), pp. 115–133.
[3] Edited by W.-H. Hucho, *Aerodynamics of Road Vehicles* (Oxford, United Kingdom, Butterworth-Heinemann, 1987).
[4] S. R. Ahmed, G. Ramm, and G. Faltin, Some salient features of the time-averaged ground vehicle wake, SAE transactions **93**, 473 (1984).
[5] G. Rigas, A. R. Oxlade, A. S. Morgans, and J. F. Morrison, Low-dimensional dynamics of a turbulent axisymmetric wake, J. Fluid Mech. **755**, R5 (2014).
[6] M. Grandemange, M. Gohlke, and O. Cadot, Statistical axisymmetry of the turbulent sphere wake, Exp. Fluids **55**, 1838 (2014).
[7] E. G. Duell and A. R. George, Experimental study of a ground vehicle body unsteady near wake, SAE transactions **108**, 1589 (1999).
[8] S. Krajnovic and L. Davidson, Numerical study of the flow around a bus-shaped body, J. Fluids Eng. **125**, 500 (2003).
[9] P. W. Bearman, Near wake flows behind two-and three-dimensional bluff bodies, J. Wind Eng. Indust. Aerodyn. **69–71**, 33 (1997).
[10] W. T. Mason and P. S. Beebe, The drag related flow field characteristics of trucks and buses, in *Aerodynamic Drag Mechanisms of Bluff Bodies and Road Vehicles* (Springer, 1978), pp. 45–93.
[11] M. Grandemange, M. Gohlke, and O. Cadot, Turbulent wake past a three-dimensional blunt body. Part 1. Global modes and bi-stability, J. Fluid Mech. **722**, 51 (2013).
[12] M. Grandemange, O. Cadot, and M. Gohlke, Reflectional symmetry breaking of the separated flow over three-dimensional bluff bodies, Phys. Rev. E **86**, 035302 (2012).
[13] G. Bouchet, M. Mebarek, and J. Dušek, Hydrodynamic forces acting on a rigid fixed sphere in early transitional regimes, Eur. J. Mech. B Fluids **25**, 321 (2006).
[14] O. Evstafyeva, A. S. Morgans, and L. Dalla Longa, Simulation and feedback control of the Ahmed body flow exhibiting symmetry breaking behaviour, J. Fluid Mech. **817**, R2 (2017).
[15] G. Rigas, A. S. Morgans, R. D. Brackston, and J. F. Morrison, Diffusive dynamics and stochastic models of turbulent axisymmetric wakes, J. Fluid Mech. **778**, R2 (2015).
[16] M. Grandemange, M. Gohlke, and O. Cadot, Bi-stability in the turbulent wake past parallelepiped bodies with various aspect ratios and wall effects, Phys. Fluids **25**, 095103 (2013).
[17] A. Kourta and C. Leclerc, Characterization of synthetic jet actuation with application to Ahmed body wake, Sens. Actuators A **192**, 13 (2013).
[18] L. Dalla Longa, O. Evstafyeva, and A. S. Morgans, Simulations of the bi-modal wake past three-dimensional blunt bluff bodies, J. Fluid Mech. **866**, 791 (2019).
[19] O. Cadot, A. Evrard, and L. Pastur, Imperfect supercritical bifurcation in a three-dimensional turbulent wake, Phys. Rev. E **91**, 063005 (2015).
[20] R. Volpe, P. Devinant, and A. Kourta, Experimental characterization of the unsteady natural wake of the full-scale square back Ahmed body: Low bi-stability and spectral analysis, Exp. Fluids **56**, 99 (2015).
[21] R. D. Brackston, J. M. García De La Cruz, A. Wynn, G. Rigas, and J. F. Morrison, Stochastic modelling and feedback control of bistability in a turbulent bluff body wake, J. Fluid Mech. **802**, 726 (2016).
[22] Y. Haffner, J. Borée, A. Spohn, and T. Castelain, Mechanics of bluff body drag reduction during transient near-wake reversals, J. Fluid Mech. **894**, A14 (2020).
[23] B. Plumejeau, L. Keirsbulck, S. Delprat, M. Lippert, and W. Abassi, Behavior of the square-back Ahmed body global modes at low ground clearance, Phys. Rev. Fluids **5**, 084701 (2020).
[24] D. Barros, J. Borée, O. Cadot, A. Spohn, and B. R. Noack, Forcing symmetry exchanges and flow reversals in turbulent wakes, J. Fluid Mech. **829**, R1 (2017).

[25] A. N. Rao, G. Minelli, J. Zhang, B. Basara, and S. Krajnović, Investigation of the near-wake flow topology of a simplified heavy vehicle using PANS simulations, J. Wind Eng. Indust. Aerodyn. **183**, 243 (2018).
[26] R. Verzicco, M. Fatica, G. Iaccarino, P. Moin, and B. Khalighi, Large eddy simulation of a road vehicle with drag-reduction devices, AIAA J. **40**, 2447 (2002).
[27] E. Serre, M. Minguez, R. Pasquetti, E. Guilmineau, G. B. Deng, M. Kornhaas, M. Schäfer, J. Fröhlich, C. Hinterberger, and W. Rodi, On simulating the turbulent flow around the Ahmed body: A French–German collaborative evaluation of LES and DES, Comput. Fluids **78**, 10 (2013).
[28] R. Pasquetti and N. Peres, A penalty model of synthetic micro-jet actuator with application to the control of wake flows, Comput. Fluids **114**, 203 (2015).
[29] J.-M. Lucas, O. Cadot, V. Herbert, S. Parpais, and J. Délery, A numerical investigation of the asymmetric wake mode of a squareback Ahmed body—Effect of a base cavity, J. Fluid Mech. **831**, 675 (2017).
[30] F. Hesse and A. S. Morgans, Simulation of wake bimodality behind squareback bluff-bodies using LES, Comput. Fluids **223**, 104901 (2021).
[31] B. Podvin, S. Pellerin, Y. Fraigneau, A. Evrard, and O. Cadot, Proper orthogonal decomposition analysis and modelling of the wake deviation behind a squareback Ahmed body, Phys. Rev. Fluids **5**, 064612 (2020).
[32] A. Evrard, O. Cadot, V. Herbert, D. Ricot, R. Vigneron, and J. Délery, Fluid force and symmetry breaking modes of a 3D bluff body with a base cavity, J. Fluids Struct. **61**, 99 (2016).
[33] M. Grandemange, M. Gohlke, and O. Cadot, Turbulent wake past a three-dimensional blunt body. Part 2. Experimental sensitivity analysis, J. Fluid Mech. **752**, 439 (2014).
[34] R. Li, D. Barros, J. Borée, O. Cadot, B. R. Noack, and L. Cordier, Feedback control of bimodal wake dynamics, Exp. Fluids **57**, 158 (2016).
[35] H.-J. Schmidt, R. Woszidlo, C. N. Nayeri, and C. O. Paschereit, The effect of flow control on the wake dynamics of a rectangular bluff body in ground proximity, Exp. Fluids **59**, 107 (2018).
[36] R. Manceau, Report on 10th Joint ERCOFTAC/IAHR/QNET-CFD Workshop on Refined Turbulence Modelling, ERCOFTAC Bulletin, Vol. 57, Univ. of Poitiers, France, 2003, pp. 36–43.
[37] S. Jakirlic, R. Jester-Zürker, and C. Tropea (eds.), *9th ERCOFTAC/IAHR/COST Workshop on Refined Turbulence Modelling, October 2–5, 2001* (Darmstadt University of Technology, Germany, 2001).
[38] TheOpenFOAMFoundation, OpenFOAM v6 User Guide, https://cfd.direct/openfoam/user-guide-v6 (2018).
[39] F. Nicoud and F. Ducros, Subgrid-scale stress modelling based on the square of the velocity gradient tensor, Flow Turbul. Combust. **62**, 183 (1999).
[40] U. Piomelli and J. R. Chasnov, Large-eddy simulations: Theory and applications, in *Turbulence and Transition Modelling* (Springer, 1996), pp. 269–336.
[41] Y. Fan, C. Xia, S. Chu, Z. Yang, and O. Cadot, Experimental and numerical analysis of the bi-stable turbulent wake of a rectangular flat-backed bluff body, Phys. Fluids **32**, 105111 (2020).
[42] R. J. A. Howard and M. J. B. M. Pourquie, Large eddy simulation of an Ahmed reference model, J. Turbul. **3**, N12 (2002).
[43] B. F. W. Gschaider, README for swak4Foam, version for OpenFOAM 2.x, https://github.com/Unofficial-Extend-Project-Mirror/openfoam-extend-swak4Foam-dev/blob/master/README (2020).
[44] Y. Eulalie, P. Gilotte, I. Mortazavi, and P. Bobillier, Wake analysis and drag reduction for a square back ahmed body using les computations, in *Proceedings of the ASME 2014 4th Joint US-European Fluids Engineering Division Summer Meeting collocated with the ASME 2014 12th International Conference on Nanochannels, Microchannels, and Minichannels. Volume 1C, Symposia: Fundamental Issues and Perspectives in Fluid Mechanics; Industrial and Environmental Applications of Fluid Mechanics; Issues and Perspectives in Automotive Flows; Gas-Solid Flows: Dedicated to the Memory of Professor Clayton T. Crowe; Numerical Methods for Multiphase Flow; Transport Phenomena in Energy Conversion From Clean and Sustainable Resources; Transport Phenomena in Materials Processing and Manufacturing Processes. Chicago, Illinois, USA, August 3–7, 2014* (ASME, 2014), p. V01CT17A010.
[45] B. Khalighi, K. Chen, and G. Iaccarino, Unsteady aerodynamic flow investigation around a simplified square-back road vehicle with drag reduction devices, J. Fluids Eng. **134**, 061101 (2012).

[46] M. Rouméas, P. Gilliéron, and A. Kourta, Analysis and control of the near-wake flow over a square-back geometry, Comput. Fluids **38**, 60 (2009).
[47] M. Minguez, R. Pasquetti, and E. Serre, High-order large-eddy simulation of flow over the Ahmed body car model, Phys. Fluids **20**, 095101 (2008).
[48] Z. Artstein, Stabilization with relaxed controls, Nonlinear Anal. Theory Methods Appl. **7**, 1163 (1983).
[49] L. Wong, F. H. Leung, and P. K. Tam, Lyapunov-function-based design of fuzzy logic controllers and its application on combining controllers, IEEE Trans. Ind. Electron. **45**, 502 (1998).
[50] L. Dalla Longa, A. S. Morgans, and J. A. Dahan, Reducing the pressure drag of a D-shaped bluff body using linear feedback control, Theor. Comput. Fluid Dyn. **31**, 567 (2017).
[51] E. Varon, J. Aider, Y. Eulalie, S. Edwige, and P. Gilotte, Adaptive control of the dynamics of a fully turbulent bimodal wake using real-time PIV, Exp. Fluids **60**, 124 (2019).
[52] M. Lorite-Díez, J. Jiménez-González, L. Pastur, C. Martínez-Bazán and O. Cadot, Experimental analysis of the effect of local base blowing on three-dimensional wake modes, J. Fluid Mech., **883**, A53 (2020).
[53] E.-C. Hsu, L. Pastur, O. Cadot, and V. Parezanović, A fundamental link between steady asymmetry and separation length in the wake of a 3D square-back body, Exp. Fluids **62**, 95 (2021).
[54] J. A. Dahan, A. Morgans, and S. Lardeau, Feedback control for form-drag reduction on a bluff body with a blunt trailing edge, J. Fluid Mech. **704**, 360 (2012).
[55] B. Khalighi, S. Zhang, C. Koromilas, S. R. Balkanyi, Luis P. Bernal, G. Iaccarino, and P. Moin, Experimental and computational study of unsteady wake flow behind a bluff body with a drag reduction device, SAE Transactions **110**, 1209 (2001).
[56] G. Rigas, L. Esclapez, and L. Magri, Symmetry breaking in a 3D bluff-body wake, arXiv:1703.07405.
[57] E. Berger, D. Scholz, and M. Schumm, Coherent vortex structures in the wake of a sphere and a circular disk at rest and under forced vibrations, J. Fluids Struct. **4**, 231 (1990).
[58] A. Lahaye, A. Leroy, and A. Kourta, Aerodynamic characterisation of a square back bluff body flow, Int. J. Aerodyn. **4**, 43 (2014).
[59] N. Kang, E. E. Essel, V. Roussinova, and R. Balachandar, Effects of approach flow conditions on the unsteady three-dimensional wake structure of a square-back Ahmed body, Phys. Rev. Fluids **6**, 034613 (2021).
[60] See Supplemental Material at http://link.aps.org/supplemental/10.1103/PhysRevFluids.7.084401 for the top-view of the projected steamlines based on the streamwise velocity at a midplane of the body height. This shows the link between the switching mechanism and the free shear layers separated off the side surfaces of the body. The inset shows the instantaneous position of the wake based of the horizontal gradient of the center of pressure.
[61] J. H. Gerrard, The mechanics of the formation region of vortices behind bluff bodies, J. Fluid Mech. **25**, 401 (1966).
[62] L. Sirovich, Turbulence and the dynamics of coherent structures. I. Coherent structures, Q. Appl. Math. **45**, 561 (1987).